

Dye-Sensitized TiO₂ Modified with Iron Polypyridyl Catalyst for
Photocatalytic Hydrogen Evolution

Wanji Zhang

Changchun, Jilin, China

Bachelor of Science, The College of William and Mary, 2015

A Thesis presented to the Graduate Faculty
of the College of William and Mary in Candidacy for the Degree of
Master of Science

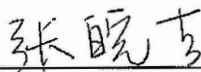
Department of Chemistry

The College of William and Mary
August, 2016

APPROVAL PAGE

This Thesis is submitted in partial fulfillment of
the requirements for the degree of

Master of Science



Wanji Zhang

Approved by the Committee, June, 2016



Committee Chair

Assistant Professor William McNamara, Chemistry
The College of William and Mary



Professor Deborah Bebout, Chemistry
The College of William and Mary



Associate Professor, Kristin Wustholz, Chemistry
The College of William and Mary

ABSTRACT

Artificial Photosynthesis (AP) focuses on finding a way to harness solar energy to generate a chemical fuel. TiO_2 semiconductors are of interest to AP research due to its relatively low cost and widespread use as an efficient charge-separating support. This research focuses on the development of a device for photocatalytic hydrogen generation. Our approach utilizes the immobilization of iron polypyridyl catalysts and ruthenium chromophores on TiO_2 through stable phosphonic acid anchoring groups.

TABLE OF CONTENTS

Acknowledgements	iii
List of Tables	iv
List of Figures	v
List of Schemes	vii
Chapter 1: Introduction	1
The Global Energy Crisis	1
From Natural Photosynthesis to Artificial Photosynthesis	5
Photocatalysis of Overall Water Splitting on Semiconductor Surfaces	7
Modification of TiO ₂ Semiconductor	9
Photocatalytic H ₂ Evolution by Hydrogenases on Dye-Sensitized	12
TiO ₂ Photocatalytic H ₂ Evolution by a Cobaloxime on Dye-Sensitized	14
TiO ₂ H ₂ Evolution Catalyzed by an Iron Polypyridyl Complex	17
References	20
Chapter 2: Immobilization of the Iron Polypyridyl Complex on TiO ₂	
Semiconductor	23
Introduction	23
Experimental Procedure	26
Results and Discussion	42
Conclusion	52

References	53
Appendix A	55
Chapter 3: Photocatalytic Hydrogen Evolution from Water with the Iron Polypyridyl Catalyst on a Dye-Sensitized TiO ₂ Nanoparticle	69
Introduction	69
Experimental Procedure	72
Results and Discussion	77
Conclusion	81
References	82

ACKNOWLEDGEMENTS

I would like to first thank Professor McNamara for his mentorship and patient guidance for the past four years. My research experience in this lab has been very challenging, and I would not be even close to where I am in this research project without your assistance and encouragement. Thank you for pushing me through all the challenges along the way. It is my source of confidence for becoming an independent researcher in the future. I also want to acknowledge all the lab members in Professor McNamara's research group for their help and support, especially Megan Screen and Sophie Padilla for their help on the daunting photochemical experiments and synthesis.

I would also like to thank Professor Bebout and Professor Wustholz for serving on my thesis committee. Professor Bebout has helped me to thrive in the graduate program. Her patient guidance on graduate study and life makes my last year at William and Mary both fun and fulfilling. I am grateful to Professor Wustholz for her guidance through Advanced Physical Chemistry. Her instruction not only opens a new perspective for scientific writing and presenting, but also encourages me to step out of my comfort zone to explore all fields of chemistry.

Finally, I would like to thank my parents and Yuyang Shi for all the support during my time at William and Mary. Thanks for traveling all the way to US when I could not go home for the past three years. Their endless support and love are my courage for pursuing my dream.

LIST OF TABLES

3.1. Hydrogen evolution from [FeCl₂(L-PO₃H₂)]/RuP sensitized TiO ₂	80
---	----

LIST OF FIGURES

1.1. Projected global transformation of energy systems	3
1.2. Z-scheme of photosynthesis	5
1.3. Energy levels of TiO ₂	7
1.4. Schematic of the water splitting dye sensitized solar cell	10
1.5. Hydrogen evolution from a [NiFeSe]-hydrogenase/ RuP sensitized TiO ₂ nanoparticle	12
1.6. Hydrogen evolution in a homogeneous system containing [Co ^{III} (dmgH ₂)pyCl]	15
1.7. Hydrogen evolution from a RuP/CoP co-sensitized TiO ₂	16
1.8. Hydrogen evolution in system containing [FeCl₂(L)]	18
1.9. TiO ₂ -based photocatalytic system containing [FeCl₂(L)]	19
2.1. TiO ₂ surface binding scheme for carboxylate and phosphonate	23
2.2. The iron polypyridyl complexes with anchoring groups	24
2.3. Cyclic Voltammograms of [FeCl₂(L-COOH)]	43
2.4. Cyclic Voltammograms of [FeCl₂(L-NH₂)]	44
2.5. Cyclic Voltammograms of [FeCl₂(L)]	47
2.6. UV-vis of RuP on TiO ₂	48
2.7. UV-vis of [FeCl₂(L-COOH)] on TiO ₂ before exposure to water and after exposure to water	49
2.8. UV-vis of [FeCl₂(L-PO₃H₂)] on TiO ₂ before exposure to water and after exposure to water	50
3.1. Hydrogen evolution with [FeCl₂(L-PO₃H₂)]/ RuP sensitized TiO ₂	70

3.2. Calibration curve of H ₂ to CH ₄ peak areas	75
3.3. UV-vis spectrum of L-PO₃H₂ solution in methanol	77
3.4. UV-vis spectrum of L-PO₃H₂ supernatant after stirring with TiO ₂	78
A1. ¹ H NMR spectrum of 1	55
A2. ¹³ C NMR spectrum of 1	55
A3. High-resolution mass spectrum of 2	56
A4. ¹ H NMR spectrum of 3	56
A5. ¹³ C NMR spectrum of 3	57
A6. ¹ H NMR spectrum of 4	57
A7. ¹³ C NMR spectrum of 4	58
A8. High-resolution mass spectrum of 4	58
A9. ¹ H NMR spectrum of 6	59
A10. ¹³ C NMR spectrum of 6	59
A11. ¹ H NMR spectrum of 7	60
A12. High-resolution mass spectrum of 8	60
A13. ¹ H NMR spectrum of 9	61
A14. ¹ H NMR spectrum of 10	61
A15. ¹ H NMR spectrum of 11	62
A16. ¹³ C NMR spectrum of 11	62
A17. GC-MS spectrum of 11	63
A18. ¹ H NMR spectrum of 12	63
A19. ¹³ C NMR spectrum of 12	64
A20. High-resolution mass spectrum of 12	64

A21. ^1H NMR spectrum of 13	65
A22. ^{13}C NMR spectrum of 13	65
A23. High-resolution mass spectrum of 13	66
A24. ^1H NMR spectrum of 14	66
A25. ^{13}C NMR spectrum of 14	67
A26. ^1H NMR spectrum of 15	67
A27. ^1H NMR spectrum of 16	68
A28. ^1H NMR spectrum of 17	68

LIST OF SCHEMES

1.1. The redox potentials of the two half reactions of water splitting	6
2.1. Synthesis of [FeCl₂(L)]	26
2.2. Synthesis of [FeCl₂(L-COOH)]	28
2.3. Synthesis of [FeCl₂(L-NH₂)]	30
2.4. Synthesis of 10	32
2.5. Synthesis of 11	33
2.6. Synthesis of L-PO₃H₂	34
2.7. Synthesis of 14	36
2.8. Synthesis of RuP	38
2.9. Functionalize the ligand with phosphonate anchoring group	45
2.10. Loading TiO ₂ films with [FeCl₂(L-PO₃H₂)]	46

Chapter 1 Introduction

The Global Energy Crisis

With global industrialization and rapid population growth, the world has seen a dramatic increase in energy demands over the past few decades. Between 1973 and 2013, global energy consumption has grown from 15.1 TW to 30.0 TW.¹

According to the International Energy Agency's projection of global energy trends, energy demand will increase by at least 33% before 2040, driven mainly by the energy needs of emerging markets such as China and India.⁹ In order to meet the growing scale of annual consumption, a transformed energy system including more renewable sources would be ideal. However, since the Industrial Revolution, the primary energy sources have always been non-renewable fossil fuels such as oil, natural gas, and coal. While the role of renewable energy has increased significantly, fossil fuels still account for 81.4% of the global energy consumption in 2013, and it will continue to provide the majority of the energy shares for the foreseeable future.^{1, 9-10}

The global reliance on fossil fuels raises the question of sustainability. Although fossil fuel resources are abundant in many regions of the world, most of them are not classified as reserves.¹¹ The distinction is important because only the proven reserves can be extracted with available technologies and be brought to the market. The estimated years of reserves left, based on current consumption levels, is in the range of 40 to 45 years for oil, 60 to 65 years for natural gas, and 230 years for coal.¹¹⁻¹² As the techniques for extracting fossil fuels develop, more resources can be converted into reserves, and these periods

will most likely be extended. However, the yearly increase of deep mining and oil drilling has brought along with it the potential danger to the environment. For example, on April 20, 2010, the Deepwater Horizon drilling rig in the Gulf of Mexico exploded, injecting 2,900,000 L of oil near the seafloor.¹³ The accident not only took the lives of 11 workers, but also caused disastrous impact on the environment. Since the oil was spilled in deep water, the water-soluble petroleum compounds will spend a significant residence time in the water with no opportunity to volatilize to the atmosphere.¹⁴ The spill led to the immediate deaths of countless marine animals and vegetation, and a long-term environmental collapse on a massive scale.¹⁵

Despite the limited proven reservoirs and the safety issues coming along with deep exploitation, fossil fuels are sufficient in quantities to meet the increasing global energy demands for the next hundreds of years.¹² The problem for the immediate future is not exhaustion of fossil fuels, but the consequences of its combustion.¹⁶ Indeed, the combustion of fossil fuels during energy production has led to serious environmental problems such as air pollution and global warming, which are currently major threats to both public health and the ecosystem.¹⁷

Fossil fuels usually contain nitrogen and sulfur impurities. During combustion, these compounds are converted to corrosive and toxic nitrogen/sulfur oxides, which can form acid rain when dissolved in rain water. In addition, particulate matters (PM) can also be emitted when fossil fuels are burnt. These particle complexes contain microscopic solids and liquid droplets that can

get into lungs and cause serious diseases such as respiratory illness, cardiovascular diseases and cancer.¹⁸ The accumulating evidence has made it hard to dismiss the effects of air pollution on the public health. According to the World Health Organization (WHO), indoor and outdoor air pollution is the sixth-leading cause of death, contributing each year to approximately 800,000 deaths and 4.6 million lost lives worldwide.¹⁹ The resulting increase in hospitalizations, work-day lost, and school-days lost also has a great impact on economy and social stability.¹⁸

Combustion of fossil fuels also leads to the risk of global warming. CO₂ comprises 90% of energy-related emission.²⁰ It has the ability to absorb infrared radiation emitted by the earth and re-radiate it back, which is known as the greenhouse effect. As the atmospheric concentrations of CO₂ increases, the greenhouse effect intensifies and ultimately leads to global warming.^{17, 21} CO₂ is

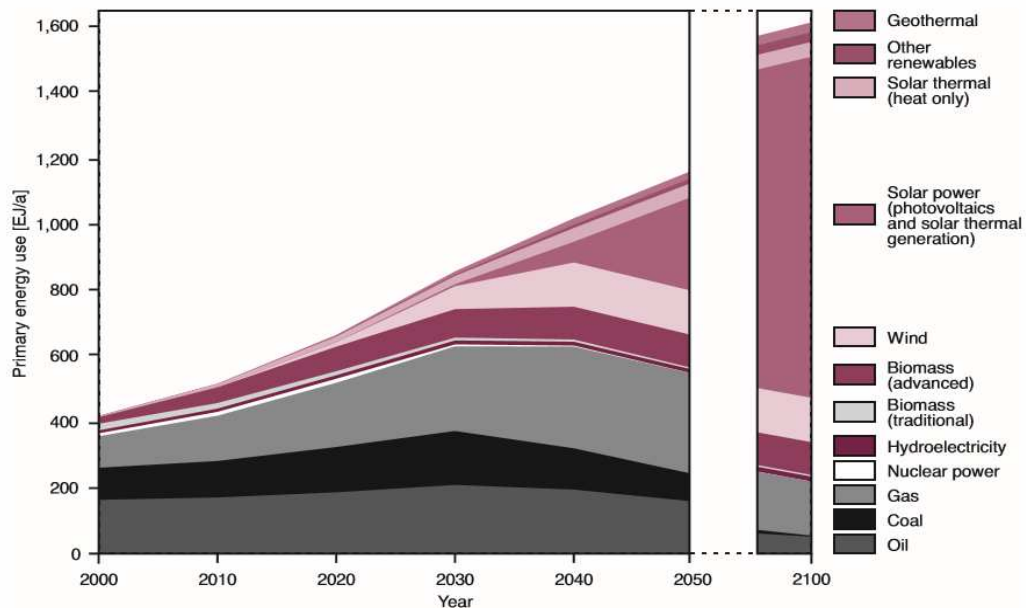


Figure 1.1. Projected global transformation of energy systems until 2050/2100.²

very stable in the atmosphere causing a long-lasting warming effect. Compare with 1990, global CO₂ emission increased by over 50%, at an accelerating annual rate of 2.3%.²⁰ Correspondingly, the average temperature of the earth has increased 1.4°F since 1880.²² Anticipated effects of global warming include, but are not limited to, heat stress, frequent extreme weather, increasing ocean acidity, rising sea levels, and melting of glaciers, all of which can severely damage the ecosystem.¹⁸

Since air pollution and global warming are primarily the consequences of fossil fuel combustion, they can only be addressed with large scale changes of the energy sectors to clean, renewable sources.¹⁸ Figure 1.1 illustrates the projection of German Advisory Council on Global Change (WBGU) on the global energy transformation path until 2050/2100.² In the next 100 years, the major trends of the exemplary path are significant reduction in the use of fossil fuels, and substantial expansion of renewable energy sources, including geothermal, solar, wind, biomass and hydroelectricity. Notably, solar power will most likely become the primary energy source in the future due to the enormous amount of energy available to us from solar radiation. With 1.2×10^5 TW of solar energy striking the surface of the earth in a year, it can easily meet the 30 TW annual consumption if we are able to capture it.²³ Active solar techniques, such as solar photovoltaics (PVs), concentrated solar power and solar thermal collectors, are able to convert solar radiation into direct current electricity. However, they cannot store the energy for later use. Among all the proposed methods of harnessing

solar energy, an especially attractive approach is to store it in the form of chemical bonds as occurs in natural photosynthesis.¹⁶

From Natural Photosynthesis to Artificial Photosynthesis

The energy capturing reaction of photosynthesis plays a crucial role in converting solar energy into chemical energy, which fuels green plants with carbohydrates, and ultimately sustains all life on earth. Through photosynthesis in green plants and photosynthetic bacteria, CO₂ and water are consumed to produce O₂ and carbohydrates via a series of photochemical reactions and dark catalytic reactions (Calvin Cycle).^{3, 7} There are two related photosystems in

photosynthesis (Figure 1.2): Photosystem I (PSI) and Photosystem II (PSII).^{3, 7}

Upon solar irradiation, the light energy is absorbed by chlorophyll and other pigments in PSI. The captured energy is transferred efficiently to the PSI reaction center to induce a charge-separated state, which drives the reduction of a series of electron acceptors, such as, plastoquinone and ferredoxin, ultimately reducing the cofactor NADP⁺ (nicotinamide adenine dinucleotide phosphate) to NADPH (biological hydrogen).^{3, 7, 16} By utilizing NADPH as both the electron source and the proton source, CO₂ is transformed into carbohydrates in the Calvin Cycle.

The reduction of the cofactor results in an oxidized PSI, which is regenerated by

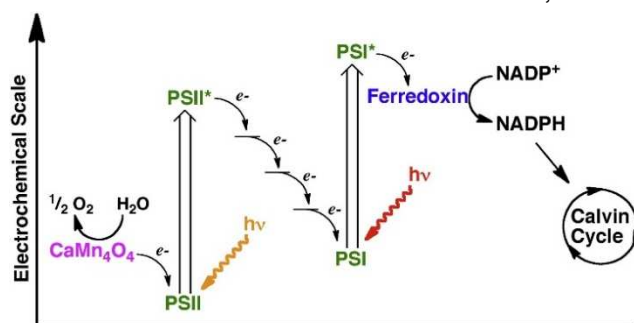
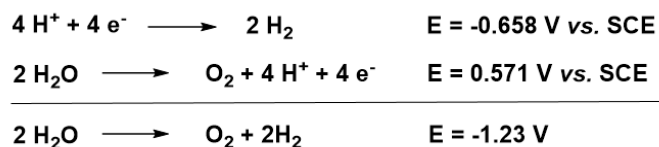


Figure 1.2. A simplified Z-scheme of the light reactions of photosynthesis.⁷

photo-induced electron transfer from PSII. The oxidized PSII drives the water splitting reaction to produce O₂, catalyzed by a CaMn₄O₄ cluster.^{3, 7}

Inspired by nature, the high specific energy carrier H₂, a renewable carbon-free fuel, can be produced from sunlight and water by using principles adopted from the NADPH production process.²⁴ Similar to photosynthesis, Artificial Photosynthesis (AP) is essentially a photochemical water splitting process that can be divided into two half reactions (Scheme 1.1): the reduction of water to H₂, and the oxidation of water to O₂. In an AP system, a light absorber absorbs a



Scheme 1.1. The redox potentials of the two half reactions of water splitting at pH 7 vs. SCE.³

photon to induce a charge-separated state. The excited electron is stabilized by an electron relay or a pathway that proceeds favorably in one direction to drive the H₂-forming cathodic process.⁷ To complete the redox cycle of water splitting, electrons are extracted from water itself in a four-electron process to release O₂.²⁴ According to the redox potentials of the two half reactions (Scheme 1.1), electrochemical water splitting requires a potential difference greater than 1.23 V between the electrodes, which corresponds to the energy of light with a wavelength of approximately 1000 nm.³ Therefore, if the energy of light is used efficiently, photochemical decomposition of water with visible light is theoretically possible.²⁵

Photocatalysis of Overall Water Splitting on Semiconductor Surfaces

Semiconductors are attractive candidates for heterogeneous photocatalysis of water splitting because they can undergo band-gap photoexcitation, generating a charge-separated state. A semiconductor consists of a conduction band (CB) and a valence band (VB). The region from the top of VB to the bottom of CB is called the band gap. In the resting state of a semiconductor, both electrons and holes are in VB. Upon photoexcitation, if the photons have energy equal or larger than the band gap energy level, the electrons will be promoted to CB, leaving a photo-generated hole in VB. Unlike the continuous electronic states of a conductor, the band gap in a semiconductor is a void energy region where no energy levels are allowed for electron/hole recombination.²⁶ Therefore, once the photoexcitation occurs, some of the electron-hole pairs have sufficient lifetime to migrate to the surface of the semiconductor without recombination.²⁷ These electrons and holes can reduce or oxidize the absorbed reactants on the semiconductor respectively.

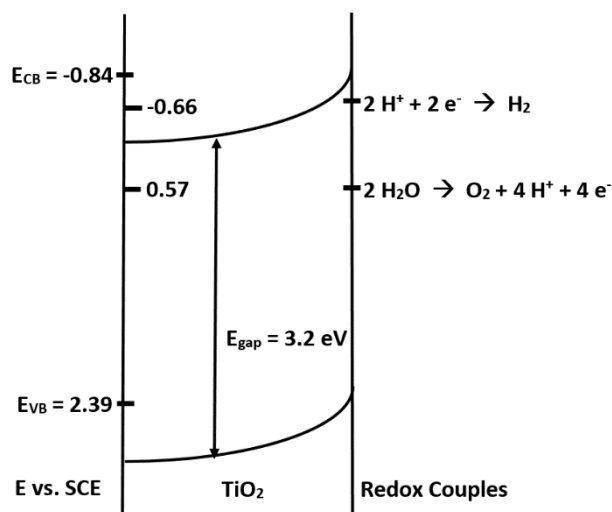


Figure 1.3. Energy levels of TiO_2 and the redox potentials of water splitting half reactions.⁴

The ability of semiconductor to transfer photo-induced electrons/holes to the absorbed reactant depends on the CB and VB energy positions and the redox potential of the reactant.²⁶ Photocatalysis of water splitting on semiconductor can be energetically favorable if the CB level is more negative than the proton reduction potential, and the VB level is more positive than the water oxidation potential (Figure 1.3).⁴ Among all types of semiconductors that meet the above criteria, TiO_2 semiconductors are of special interest to water splitting research due to their relatively low cost, stability, and widespread use as an efficient charge-separation carrier.²⁸

In 1972, Fujishima and Honda reported the first example of photocatalytic water splitting on a TiO_2 electrode.²⁵ In the Fujishima-Honda Cell, a TiO_2 electrode is connected to a Pt electrode through an external circuit. When the surface of the TiO_2 electrode is irradiated by light with a wavelength shorter than 415 nm, water is oxidized to O_2 at the TiO_2 electrode, and protons are reduced to H_2 at the Pt electrode with the application of a small external voltage ($> 0.25 \text{ V}$).²⁹ The Fujishima-Honda cell established TiO_2 as the most promising heterogeneous photocatalyst for overall water splitting. However, the following issues greatly compromise the quantum yield of the system: (1) Fast photo-generated electron/hole pairs recombination: most of the photo-generated electrons and holes recombine radiatively or non-radiatively before participating in redox reactions. A small bias voltage is necessary to assist efficient water splitting; (2) inability to utilize visible light: the band gap of TiO_2 is 3.2 eV, which means the system only works under UV illumination. Since UV light only accounts for 4% of

the solar radiation, the efficiency of the water splitting is limited; (3) high overpotential for H_2 and O_2 evolution: the water splitting reaction has a large activation barrier. Therefore, only a small amount of electron/hole pairs generated by photoexcitation have sufficient energy to drive the reaction, which is detrimental to the rate of photocatalysis.³⁰

In order to overcome the above limitations of TiO_2 semiconductor as a photocatalyst for water splitting, extensive research has been performed on modifying the surface of TiO_2 .²⁶ Dye-sensitization of TiO_2 can significantly enhance the visible light response; co-attachment of H_2/O_2 production catalyst can lower the activation barrier to promote the photocatalytic efficiency.²⁷ To date, several examples have been reported illustrating surface sensitization of TiO_2 with dye molecules and/or electrocatalysts as effective techniques to improve the activity of the TiO_2 -based water splitting system.^{6, 10, 24}

Modification of TiO_2 Semiconductor

In 2008, Mallouk and coworkers reported a dye-sensitized TiO_2 -based photoelectrochemical cell for photocatalytic overall water splitting.⁶ The system employed a Ru(III) tris(bipyridine) derivative as both a stabilizer for the water oxidation catalyst $\text{IrO}_2 \cdot n\text{H}_2\text{O}$ and a photosensitizer (Figure 1.4). The dye- $\text{IrO}_2 \cdot n\text{H}_2\text{O}$ colloid was absorbed onto a TiO_2 electrode through its phosphonic acid anchors. The modified TiO_2 electrode is connected with a Pt electrode through an external circuit. Upon irradiation with visible light, electron injection is observed from the Ru dye into the CB of TiO_2 . The electron ultimately reduces water into hydrogen on the surface of the Pt electrode. Accordingly, electron

transfers from $\text{IrO}_2 \cdot n\text{H}_2\text{O}$ to the oxidized Ru dye and generates a hole on $\text{IrO}_2 \cdot n\text{H}_2\text{O}$, which is scavenged by water oxidation.

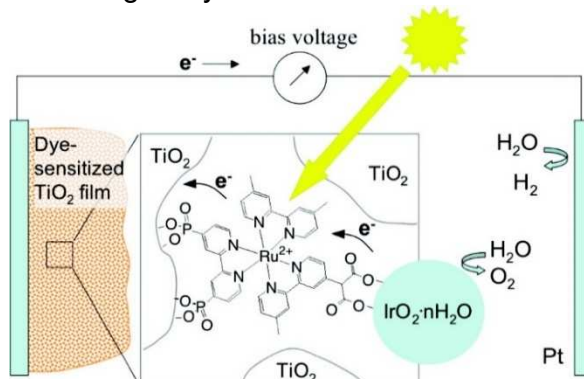


Figure 1.4. Schematic of the water splitting dye sensitized solar cell.⁶

This dye-sensitized solar cell successfully extends the TiO_2 light absorbance range from UV to visible region. However, the internal quantum yield is only $\sim 0.9\%$ due to the competition between electron transfer from $\text{IrO}_2 \cdot n\text{H}_2\text{O}$ to the oxidized dye, and the back electron transfer from TiO_2 to the dye.³¹ The incorporation of Pt and IrO_2 catalysts for H_2 and O_2 evolution is another main drawback of the system since these are non-sustainable noble metals. It has been widely acknowledged that replacing the noble metal catalysts with earth abundant metal complexes for both half reactions is the key challenge towards large scale AP applications.

In order to rapidly screen suitable catalysts for H_2 and O_2 evolution, a sacrificial electron donor (e.g. ascorbic acid, TEA, TEOA) or acceptor (e.g. persulfate) is often coupled to an AP system. These sacrificial compounds can undergo irreversible decomposition upon oxidation or reduction to remove the complication of back electron transfer.⁷ Sacrificial species are extremely useful in mechanistic studies of molecular catalysts because they allow one to investigate light-driven half reactions (water oxidation or reduction) in isolation.³¹ For

example, in reductive water splitting, reduction of photoexcited Ru(III) tris(bipyridine) photosensitizer by TEOA allows continuous electron injection into the CB of TiO₂ with a well-defined potential, which is beneficial for the kinetic studies of hydrogen evolution by different catalysts.³²

A good molecular catalyst for water splitting should meet the following requirements: (1) utilize first-row, earth-abundant metals such as Fe, Co, Ni and Mo; (2) be stable in aqueous solution without undergoing ligand exchange in the active intermediate states; (3) exhibit high turnover frequency (TOF) and low overpotential. Developing a TiO₂-based system with a suitable catalyst for water oxidation is more challenging, because this half reaction is a four-electron process coupled with dioxygen bond formation and reducing equivalent generation.¹⁶ However, an active and robust system for water reduction with the minimal overpotential displayed by Pt has not been developed for practical AP applications up to this point.^{7, 10} Therefore, research has been focusing on the development of molecular catalysts for reductive water splitting. Different series of Fe, Ni and Co complexes have been demonstrated as active electrocatalysts for proton reduction. Some of them have been incorporated into TiO₂-based systems for photocatalytic hydrogen evolution.³ In the following section, photocatalytic hydrogen evolution by hydrogenase and cobaloxime on dye-sensitized TiO₂ are discussed in detail.

Photocatalytic H₂ Evolution by Hydrogenases on Dye-Sensitized TiO₂ Nanoparticles

Hydrogenases are Fe/Ni-containing microbial enzymes that catalyze the reversible interconversion of H₂ and 2H⁺/2e⁻ close to the thermodynamic potential with high TOFs.¹⁶ These enzymes are generally classified into [NiFe]-, [FeFe]-, and [Fe]-hydrogenases based on the metal composition of their active sites.³³ Previous research has shown that hydrogenases are as electrocatalytically active for hydrogen evolution and uptake as Pt nanoparticles are, which makes them promising biological alternatives in AP system.³⁴ However, since hydrogenases first evolved in anaerobic bacteria, their unsaturated metal sites at the active centers are very sensitive to the presence of oxygen. O₂ molecules are potential competitors for H₂ binding sites because both O₂ and H₂ act as π -back-donating ligands. Once a O₂ molecule binds to the active site, it can further react as an oxidant, and irreversibly deactivate the hydrogenases.³³ This limits the application of hydrogenases in AP systems since the O₂ generated during water splitting can potentially deactivate their catalytic activities.³³

In 2009, Armstrong and coworkers reported a [NiFeSe]-hydrogenase isolated from *Desulfomicrobium baculatum* that contains a terminal

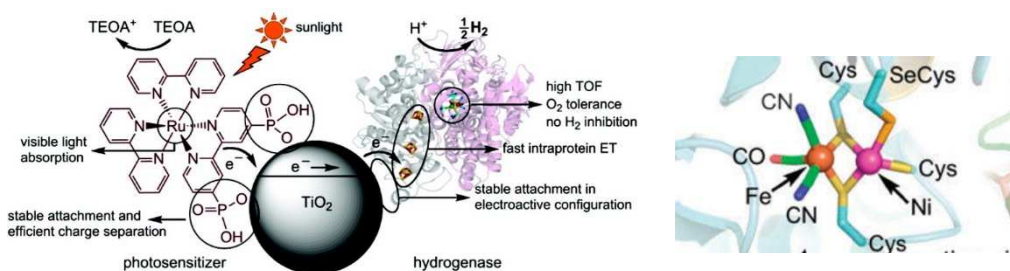


Figure 1.5. Left: Schematic of hydrogen evolution in a TiO₂-based photocatalytic system. The TiO₂ nanoparticle is sensitized with a [NiFeSe]-hydrogenase and RuP.⁸ Right: The active site of [NiFeSe]-hydrogenase.¹⁰

selenocysteine coordinated to Ni at the [NiFe]-active site.⁸ This subclass of [NiFe]-hydrogenases is not only more active for H₂ evolution, but also electrocatalytically more stable to O₂ than normal [NiFe]-hydrogenases are.⁸ This observation led to the assembling of a solar hydrogen production system consisting of direct adsorption of [NiFeSe]-hydrogenase via [4Fe4S]-cluster to TiO₂ nanoparticles sensitized with [Ru(bpy)₂(dpbpy)]Br₂ (**RuP**) (Figure 1.5).¹⁰ The fully assembled particles were irradiated in pH 7 TEOA buffer solution at 20 °C under anaerobic conditions. The system showed an initial TOF of 20 s⁻¹, and it decreased overtime due to photo instability of the system. After 8 h, the system achieved a turnover number (TON) of 1.9 × 10⁵, which corresponds to an accumulation of 4.6% H₂ in the reaction atmosphere.⁸

Armstrong and coworkers successfully demonstrated the suitability of using hydrogenases in a TiO₂-based photocatalytic system. However, the system has proved to be impractical in terms of the levels of activity and robustness for real development of a AP system. The protein environment that functions to tune the catalytic activity of the hydrogenase is unstable. The [NiFeSe]-hydrogenase can lose 20% of its catalytic activity within 48 h even under anaerobic conditions.^{8, 16} Although [NiFeSe]-hydrogenase remains somewhat electrocatalytically active after exposure to air, irradiation of the fully assembled particles in air resulted in their instantaneous and complete deactivation within only 2 min.¹⁰ The difficulties in microorganism cultivation and hydrogenase isolation are other important obstacles toward a large scale application.¹⁶

Despite the difficulties of using hydrogenases directly in hydrogen generation, it is still valuable to study the structures of their active sites and the electrocatalysis mechanisms. The remarkable catalytic activities of hydrogenases and their utilization of Fe/Ni in the active sites make them great models for developing synthetic molecular catalysts for hydrogen generation with earth abundant metals. In fact, considerable progress has been made with regard to this challenge and several functional catalysts containing Ni, Co or Fe have been reported.¹⁶ These artificial hydrogenases are not only catalytically active for hydrogen evolution, but also more robust than natural hydrogenases.⁷ Great efforts have been made to incorporate these catalysts into a dye-sensitized TiO₂ system for photocatalytic hydrogen generation.

Photocatalytic H₂ Evolution by a Cobaloxime on Dye-Sensitized TiO₂

Nanoparticles

Bis(dimethylglyoximate)cobalt complexes (cobaloximes) have long been studied as a model compound of Vitamin B₁₂ active site.⁷ In 1983, Lehn and coworkers reported one of the earliest examples using a cobaloxime-based catalyst for water reduction.^{3, 35} Their discovery sparked interest in using cobaloximes to catalyze hydrogen evolution. Among cobaloximes that have been investigated as electrocatalysts for proton reduction, [Co^{III}(dmgH)₂pyCl] (Fig. 6) is able to reduce protons in DMF at moderate potential (-0.94 V/SCE) with only 30 mV of overpotential.³⁶ Bulk electrolysis on a graphite electrode at -0.94 V/SCE yielded over 100 TONs in 2.5 h without degradation of the catalyst. The high efficiency

and robustness of $[\text{Co}^{\text{III}}(\text{dmgH})_2\text{pyCl}]$ makes it a possible alternative for hydrogenases for the reductive side of AP.

While electrochemical study provides promising overpotential and catalytic activity of the Co complex, it does not guarantee hydrogen evolution from aqueous environment in photochemical studies, where the potential at which the reducing electron is supplied to the Co complex is determined by the excited state of the photosensitizer and the sacrificial electron donor.⁷ Based on the success found on the electrochemistry of $[\text{Co}^{\text{III}}(\text{dmgH})_2\text{pyCl}]$, Eisenberg and coworkers investigated a homogeneous photocatalytic H_2 production from water incorporating the Co catalyst (Figure 1.6).⁵ The system contains Eosin Y as the photosensitizer, $[\text{Co}^{\text{III}}(\text{dmgH}_2)\text{pyCl}]$, and triethanolamine (TEOA) as the sacrificial electron donor in 1:1 MeCN/ H_2O solution at pH 7. Upon irradiation with visible light, 360 TONs were obtained in this system with a quantum yield of 4% in 5 h. Further studies revealed that the presence of excess dmgH_2 ligand extended the durability of the system to 12 h with over 900 TONs obtained. This improvement of system lifetime with excess dmgH_2 ligand suggests that ligand exchange is occurring during photocatalytic H_2 generation. After 12 h, the system stops generating hydrogen due to photo bleaching of the photosensitizer. The photo bleaching is most likely caused by the decomposition of catalyst at the ligand.

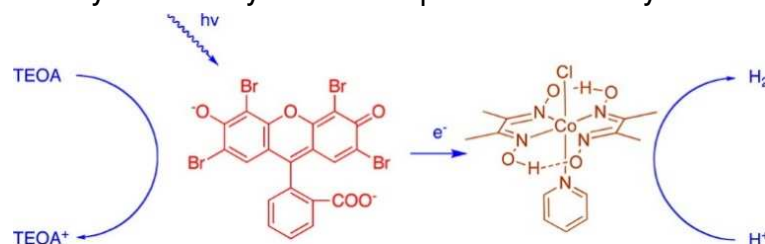


Figure 1.6. Schematic of hydrogen evolution from water in a noble-metal-free homogeneous system containing Eosin Y, $[\text{Co}^{\text{III}}(\text{dmgH}_2)\text{pyCl}]$, and TEOA.⁵

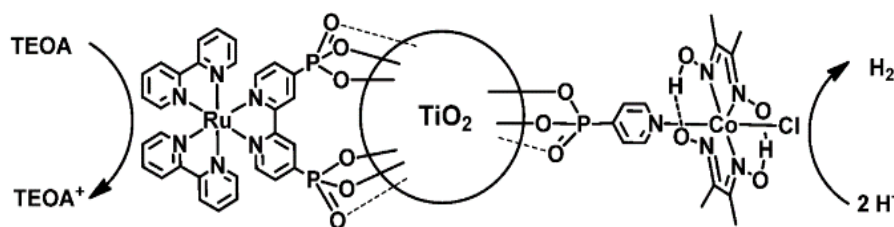


Figure 1.7. Schematic of hydrogen evolution from a **RuP/CoP** co-sensitized TiO_2 nanoparticle with TEOA as the sacrificial electron donor.³

A heterogeneous photochemical system based on TiO_2 was described shortly thereafter by Reisner and coworkers using **RuP** as the photosensitizer, $[\text{Co}^{\text{III}}(\text{dmgH})_2(\text{pyridyl-4-hydrophosphonate})\text{Cl}]$, **CoP**, as the catalyst, and TEOA as the sacrificial electron donor.²⁴ Both the **RuP** and the **CoP** are immobilized on the surface of TiO_2 via their phosphonate groups (Figure 1.7). Upon irradiation with visible light in water at pH 7, the **RuP** absorbs a photon and injects an electron into the CB of TiO_2 , from which the electron can migrate to the **CoP** and reduce H_2O to H_2 . Initially, the system produces a low TOF of 0.005 s^{-1} . The activity of the system starts decreasing after 2 h, and ceased after 8 h, resulting in 53 TONs with a quantum yield of only 1%. The poor durability of the system is probably due to ligand exchange observed in the homogeneous photocatalytic system.⁷

The **RuP/CoP** – TiO_2 system demonstrates that a first-row transition metal complex can replace Pt and hydrogenases to catalyze the hydrogen evolution from pH neutral water on TiO_2 . Kinetic studies show that photoexcitation can generate a very long-lived CB electron, and the charge-recombination with the oxidized **RuP** is much slower than electron uptake by the **CoP**, which makes a high internal electron-transfer efficiency.³⁷ Although the TOF of the **CoP** is low

compared to that of [NiFeSe]-hydrogenase, the investigation of [Co^{III}(dmgH₂)pyCl] as an electrocatalyst in both homogeneous and heterogeneous systems provide a solid basis for future research on inexpensive synthetic H₂ evolution catalysts in a TiO₂-based AP system.

H₂ Evolution Catalyzed by an Iron Polypyridyl Complex

While several Ni and Co complexes have been reported to catalyze the generation of hydrogen effectively in photocatalytic systems, the utilization of Fe is of more interest because it is the most abundant transition metal on earth. In 2014, we reported an iron polypyridyl complex, **[FeCl₂(L)]**, that was one of the most active iron electrocatalyst for proton reduction.³⁸ The structure of **[FeCl₂(L)]** is inspired by the active site of [Fe]-hydrogenase. A tetradentate monophenolate ligand is bound to iron to improve the stability of the complex (Figure 1.8). A catalytic event occurs at -1.17 V vs SCE with a 660 mV overpotential and a TOF of 1000 s⁻¹ in CH₃CN. Since the goal is to develop a catalyst for hydrogen evolution from water in an AP system, **[FeCl₂(L)]** should ideally be able to reduce protons in aqueous environment. Interestingly, **[FeCl₂(L)]** is more active in the presence of water, giving an impressive TOF of 3000 s⁻¹ with an overpotential of 800 mV in 1:1 CH₃CN/H₂O. The catalytic activity of **[FeCl₂(L)]** was also investigated in citrate-buffered systems, showing a catalytic reduction wave in pH 3-5. These results further confirmed that **[FeCl₂(L)]** is stable and active in pure aqueous environment.

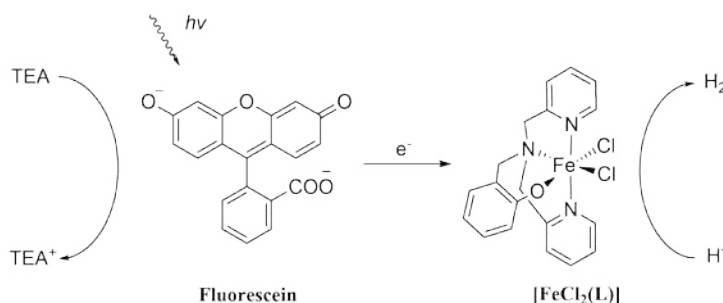


Figure 1.8. Schematic of hydrogen evolution of a homogeneous system containing **[FeCl₂(L)]**.

Based on the success found on the electrochemical studies, we investigated photocatalytic hydrogen evolution from in a homogeneous aqueous solution system incorporating **[FeCl₂(L)]** (Figure 1.8). The system contained fluorescein as the photosensitizer, **[FeCl₂(L)]** as the hydrogen evolution catalyst, and triethylamine (TEA) as the sacrificial electron donor in 1:1 EtOH/H₂O. Upon irradiation with visible light at pH 12.5, 2100 TONs were obtained in 24 h with a quantum yield of 3.1%. Interestingly, there was only a small decrease in the rate of hydrogen evolution over the period of 24 h. Further investigation shows that addition of fluorescein to the system can effectively recover the evolution rate. These results suggest that the decrease in hydrogen evolution rate is most likely caused by photo bleaching. **[FeCl₂(L)]** is both highly active and stable for photocatalytic proton reduction in aqueous solution.

The work presented in this thesis aims at attaching **[FeCl₂(L)]** to a dye-sensitized TiO₂ nanoparticle for visible light driven hydrogen evolution. The system incorporates **RuP** as the photosensitizer and a sacrificial electron donor as shown in previous similar studies (Figure 1.9). The goal of this research is to first immobilize **[FeCl₂(L)]** on TiO₂ through a stable anchoring group and then assemble the heterogeneous system for photocatalytic hydrogen evolution.

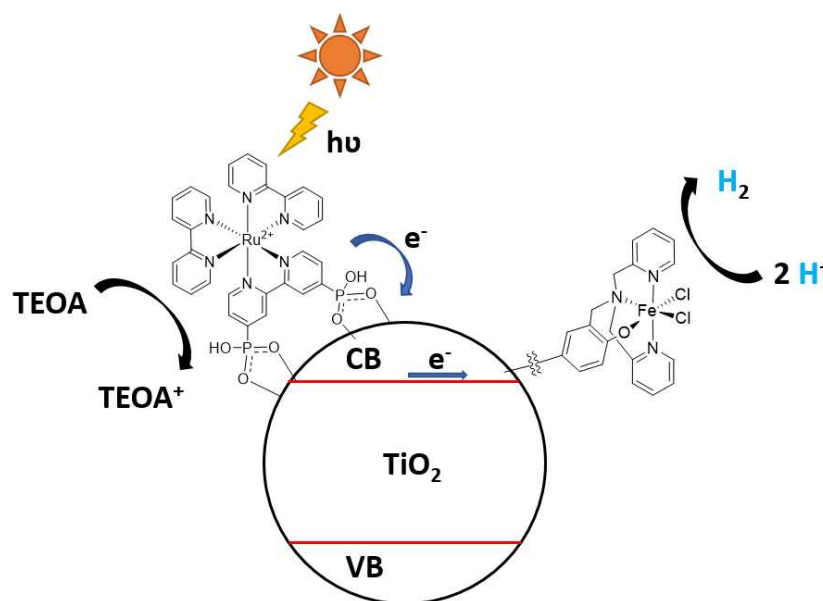


Figure 1.9. A proposed TiO₂-based photocatalytic hydrogen generation system containing **[FeCl₂(L)]**.

References

1. Key World Energy Statistics. 2015. International Energy Agency.
https://www.iea.org/publications/freepublications/publication/KeyWorld_Statistics_2015.pdf (accessed May 12, 2016).
2. Wiedemann, T., World in Transition: Towards Sustainable Energy Systems. *Int. J. Environ. Pollut.* **2006**, 27, 269-270.
3. Du, P.; Eisenberg, R., Catalysts Made of Earth-Abundant Elements (Co, Ni, Fe) for Water Splitting: Recent Progress and Future Challenges. *Energy Environ. Sci.* **2012**, 5 (3), 6012-6021.
4. Jaeger, C. D.; Bard, A. J., Spin Trapping and Electron Spin Resonance Detection of Radical Intermediates in the Photodecomposition of Water at Titanium Dioxide Particulate Systems. *J. Phys. Chem.* **1979**, 83 (24), 3146-3152.
5. Lazarides, T.; McCormick, T.; Du, P.; Luo, G.; Lindley, B.; Eisenberg, R., Making Hydrogen from Water Using a Homogeneous System Without Noble Metals. *J. Am. Chem. Soc.* **2009**, 131 (26), 9192-9194.
6. Youngblood, W. J.; Lee, S.-H. A.; Kobayashi, Y.; Hernandez-Pagan, E. A.; Hoertz, P. G.; Moore, T. A.; Moore, A. L.; Gust, D.; Mallouk, T. E., Photoassisted Overall Water Splitting in a Visible Light-Absorbing Dye-Sensitized Photoelectrochemical Cell. *J. Am. Chem. Soc.* **2009**, 131 (3), 926-927.
7. Eckenhoff, W. T.; McNamara, W. R.; Du, P.; Eisenberg, R., Cobalt Complexes as Artificial Hydrogenases for the Reductive Side of Water Splitting. *Biochimica et Biophysica Acta (BBA) - Bioenergetics* **2013**, 1827, 958-973.
8. Reisner, E.; Fontecilla-Camps, J. C.; Armstrong, F. A., Catalytic Electrochemistry of a [NiFeSe]-Hydrogenase on TiO₂ and Demonstration of its Suitability for Visible-Light Driven H₂ Production. *Chem. Commun.* **2009**, 5, 550-552.
9. World Energy Outlook 2015 Factsheet: Global Energy Trends to 2040. 2015. International Energy Agency.
http://www.worldenergyoutlook.org/media/weowebiste/2015/WEO2015_Factsheets.pdf (accessed May 12, 2016).
10. Reisner, E.; Powell, D. J.; Cavazza, C.; Fontecilla-Camps, J. C.; Armstrong, F. A., Visible Light-Driven H₂ Production by Hydrogenases Attached to Dye-Sensitized TiO₂ Nanoparticles. *J. Am. Chem. Soc.* **2009**, 131 (51), 18457-18466.
11. Resources to Reserves. 2013. International Energy Agency.
<https://www.iea.org/publications/freepublications/publication/Resources2013.pdf> (accessed May 12, 2016).
12. World Fossil Fuel Reserves and Projected Depletion. 202. The Colorado River Commission of Nevada.
<http://crc.nv.gov/docs/world%20fossil%20reserves.pdf> (accessed May 12, 2016).

13. Kujawinski, E. B.; Kido Soule, M. C.; Valentine, D. L.; Boysen, A. K.; Longnecker, K.; Redmond, M. C., Fate of Dispersants Associated with the Deepwater Horizon Oil Spill. *Environmental Science & Technology* **2011**, 45 (4), 1298-1306.
14. Reddy, C. M.; Arey, J. S.; Seewald, J. S.; Sylva, S. P.; Lemkau, K. L.; Nelson, R. K.; Carmichael, C. A.; McIntyre, C. P.; Fenwick, J.; Ventura, G. T.; Van Mooy, B. A. S.; Camilli, R., Composition and Fate of Gas and Oil Released to the Water Column during the Deepwater Horizon Oil Spill. *Proceedings of the National Academy of Sciences* **2012**, 109 (50), 20229-20234.
15. Griffin, D., Black, N., Devine C., 5 Years after the Gulf Oil Spill: What We Do (and Don't) Know. <http://www.cnn.com/2015/04/14/us/gulf-oil-spill-unknowns/> (accessed May 20, 2016)
16. Barber, J.; Tran, P. D., From Natural to Artificial Photosynthesis. *J. R. Soc. Interface* **2013**, 10 (81), 20120984/1-20120984/16.
17. Eshel, G.; Martin, P. A., Diet, Energy, and Global Warming. *Earth Interactions* **2006**, 10 (9), 1-17.
18. Jacobson, M. Z., Review of Solutions to Global Warming, Air Pollution, and Energy Security. *Energy & Environmental Science* **2009**, 2 (2), 148-173.
19. Thurston, G., Air Pollution, Human Health, Climate Change and You. *Thorax* **2007**, 62 (9), 748-749.
20. Energy and Climate Change. 2015. International Energy Agency. <https://www.iea.org/publications/freepublications/publication/WEO2015SpecialReportonEnergyandClimateChange.pdf> (accessed May 10, 2016)
21. Le Treut, H., Somerville, R., Cubasch, U., Ding, Y., Mauritzen, C., Mokssit, A., Peterson, T., Prather, M., *Historical Overview of Climate Change*. Cambridge University Press: Cambridge, United Kingdom and New York, NY, USA, 2007.
22. Global Climate Change: Vital Signs of the Planet. 2016, NASA. <http://climate.nasa.gov/> (accessed May 19, 2016).
23. Yamaguchi, M., Fara, L. *Advanced Solar Cell Materials, Technology, Modeling, and Simulation*. 2013.
24. Lakadamyali, F.; Reisner, E., Photocatalytic H₂ Evolution from Neutral Water with a Molecular Cobalt Catalyst on a Dye-Sensitized TiO₂ Nanoparticle. *Chem. Commun.* **2011**, 47 (6), 1695-1697.
25. Fujishima, A.; Honda, K., Electrochemical Photolysis of Water at a Semiconductor Electrode. *Nature* **1972**, 238 (5358), 37-38.
26. Linsebigler, A. L.; Lu, G.; Yates, J. T., Jr., Photocatalysis on TiO₂ Surfaces: Principles, Mechanisms, and Selected Results. *Chem. Rev.* **1995**, 95 (3), 735-58.
27. Ni, M.; Leung, M. K. H.; Leung, D. Y. C.; Sumathy, K., A Review and Recent Developments in Photocatalytic Water-Splitting using for Hydrogen Production. *Renewable and Sustainable Energy Reviews* **2007**, 11 (3), 401-425.

28. Ashokkumar, M., An Overview on Semiconductor Particulate Systems for Photoproduction of Hydrogen. *International Journal of Hydrogen Energy* **1998**, 23 (6), 427-438.
29. Wrighton, M. S.; Ginley, D. S.; Wolczanski, P. T.; Ellis, A. B.; Morse, D. L.; Linz, A., Photoassisted Electrolysis of Water by Irradiation of a Titanium Dioxide Electrode. *Proceedings of the National Academy of Sciences of the United States of America* **1975**, 72 (4), 1518-1522.
30. Rakowski DuBois, M.; DuBois, D. L., The Roles of the First and Second Coordination Spheres in the Design of Molecular Catalysts for H₂ Production and Oxidation. *Chemical Society Reviews* **2009**, 38 (1), 62-72.
31. Youngblood, W. J.; Lee, S.-H. A.; Maeda, K.; Mallouk, T. E., Visible Light Water Splitting Using Dye-Sensitized Oxide Semiconductors. *Accounts of Chemical Research* **2009**, 42 (12), 1966-1973.
32. Reynal, A.; Lakadamyali, F.; Gross, M. A.; Reisner, E.; Durrant, J. R., Parameters Affecting Electron Transfer Dynamics from Semiconductors to Molecular Catalysts for the Photochemical Reduction of Protons. *Energy & Environmental Science* **2013**, 6 (11), 3291-3300.
33. Vincent, K. A.; Parkin, A.; Armstrong, F. A., Investigating and Exploiting the Electrocatalytic Properties of Hydrogenases. *Chemical Reviews* **2007**, 107 (10), 4366-4413.
34. Pershad, H. R.; Duff, J. L. C.; Heering, H. A.; Duin, E. C.; Albracht, S. P. J.; Armstrong, F. A., Catalytic Electron Transport in Chromatium vinosum [NiFe]-Hydrogenase: Application of Voltammetry in Detecting Redox-Active Centers and Establishing That Hydrogen Oxidation Is Very Fast Even at Potentials Close to the Reversible H⁺/H₂ Value. *Biochemistry* **1999**, 38 (28), 8992-8999.
35. Hawecker, J.; Lehn, J.-M.; Ziessel, R., Efficient Photochemical Reduction of CO₂ to CO by Visible Light Irradiation of Systems Containing Re(bipy)(CO)₃X or Ru(bipy)₃²⁺-Co₂⁺ Combinations as Homogeneous Catalysts. *Journal of the Chemical Society, Chemical Communications* **1983**, (9), 536-538.
36. Razavet, M.; Artero, V.; Fontecave, M., Proton Electroreduction Catalyzed by Cobaloximes: Functional Models for Hydrogenases. *Inorganic Chemistry* **2005**, 44 (13), 4786-4795.
37. Lakadamyali, F.; Reynal, A.; Kato, M.; Durrant, J. R.; Reisner, E., Electron Transfer in Dye-Sensitized Semiconductors Modified with Molecular Cobalt Catalysts: Photoreduction of Aqueous Protons. *Chem. - Eur. J.* **2012**, 18 (48), 15464-15475, S15464/1-S15464/18.
38. Connor, G. P.; Mayer, K. J.; Tribble, C. S.; McNamara, W. R., Hydrogen Evolution Catalyzed by an Iron Polypyridyl Complex in Aqueous Solutions. *Inorganic Chemistry* **2014**, 53 (11), 5408-5410.

Chapter 2 Immobilization of the Iron Polypyridyl Complex on TiO₂

Semiconductor

Introduction

For photocatalytic hydrogen evolution on TiO₂ semiconductors, the TiO₂ nanoparticles are usually functionalized with photosensitizers and proton reduction catalysts to allow for visible light absorption and efficient hydrogen evolution.¹ The photosensitizers and catalysts must be covalently attached to the surface of TiO₂ to achieve electronic coupling with TiO₂ for photoinduced interfacial electron transfer (IET).³ In order to develop practical and durable artificial photosynthesis (AP) systems, the linkages bound to TiO₂ must provide a robust attachment under various conditions. Currently, suitable molecular anchors are limited to a small number of functional groups, which include carboxylic acid,⁴ phosphonates,^{1, 5} hydroxamic acid,^{3a} silanes,⁶ and acetylacetonates.⁷

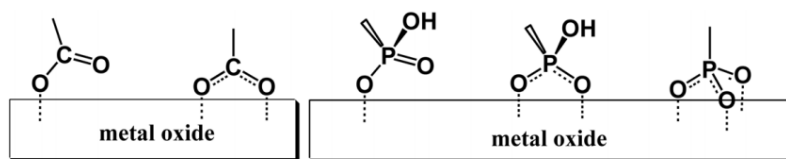


Figure 2.1. *Left:* TiO₂ surface binding scheme for carboxylic acid. *Right:* TiO₂ surface binding scheme for phosphonates.²

Carboxylate and phosphonate anchors are the most frequently used linkages for TiO₂ functionalization.⁸ Recent ATR-FTIR studies have revealed various binding mode between these anchoring groups and the surface of TiO₂.^{2, 9} A carboxylate group can coordinate to the TiO₂ surface in monodentate or as a bridging bidentate mode. For a phosphonate group, mono-, bi- and tridentate

attachments are all possible. The bidentate binding mode has been theoretically determined to be the most stable configuration (Figure 2.1).²

Although both carboxylic acids and phosphonic acids can covalently coordinate to TiO₂ surface, they exhibit very different properties in IET and stability. While carboxylic groups allow ultrafast IET between the adsorbates and TiO₂, the binding is labile in the presence of water especially in acidic pH, limiting the overall usefulness of this linkage under aqueous conditions.^{3b, 10}

Phosphonate groups can form a more robust attachment to the surface of TiO₂, but its weak electronic coupling with TiO₂ leads to a slow IET, which decreases the efficiency of AP systems.^{3b, 5a} Thus, it remains controversial as to which anchor is the most appropriate for general use in AP systems.

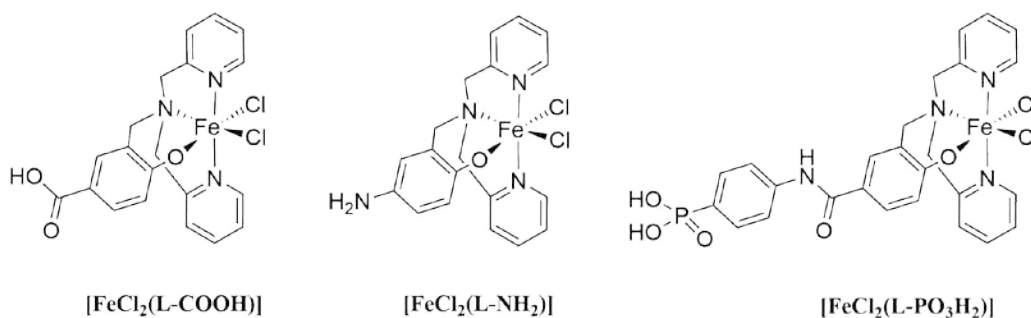


Figure 2.2. The iron polypyridyl complexes functionalized with a carboxylic acid, an amine, or a phosphonic acid group.

The goal of this chapter is to functionalize the parent catalyst **[FeCl₂(L)]** with anchoring groups while maintaining its catalytic activity for proton reduction. Due to synthetic feasibility and demonstrated utility in other AP systems, it was of

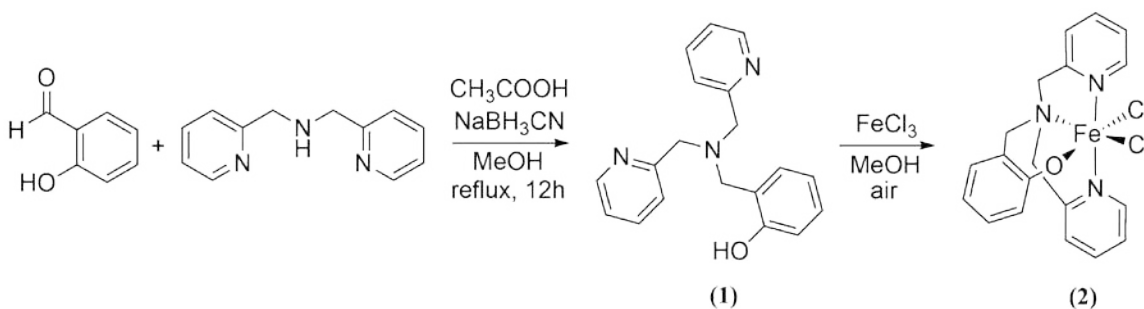
interest to incorporate a carboxylate or a phosphonate anchoring group to **[FeCl₂(L)]**.

We synthesized an iron complex **[FeCl₂(L-COOH)]** with a carboxylic acid anchoring group to bind to the TiO₂ surface (Figure 2.2). We further demonstrated that **[FeCl₂(L-COOH)]** is catalytically active for proton reduction using cyclic voltammetry (CV). Additionally, it was shown that the complex can form a stable attachment to TiO₂ in non-aqueous environment. In order to investigate the stability of the carboxylic acid anchoring group under aqueous condition, we sensitized TiO₂ thin films with **[FeCl₂(L-COOH)]** and measured the desorption of the complex from TiO₂ surface after exposure to water. Diffuse reflectance UV/vis spectroscopy indicated that the carboxylic acid binding of **[FeCl₂(L-COOH)]** to TiO₂ was not stable in water.

An iron complex **[FeCl₂(L-NH₂)]** was also synthesized (Figure 2.2). It bore a primary amine functional group for coupling to a molecular phosphonate linker. While the CV results showed that the complex was highly active for proton reduction, the attempt to couple the complex to the phosphonate linker failed. Therefore, **[FeCl₂(L-PO₃H₂)]** with a phosphonic acid anchoring group was synthesized (Figure 2.2). UV-vis studies demonstrated that the phosphonic acid anchoring group on **[FeCl₂(L-PO₃H₂)]** can provide more stability when bound to TiO₂ surface than the carboxylic acid on **[FeCl₂(L-COOH)]**.

Experimental Procedure

Sample preparation and experimental procedures are described below. All synthesis experiments were performed using standard air-free Schlenk techniques under Ar atmosphere unless noted otherwise. All reagents not specifically mentioned were purchased from Acros Organics, Strem Chemicals, TCL, Alfa Aesar, or Fisher Scientific without further purification. The Degussa P25 TiO₂ nanoparticles are 25 nm in diameter and are 70% anatase and 30% rutile. ¹H and ¹³C spectra were obtained using an Agilent 400MR DD2 spectrometer operating in the pulse Fourier transform mode. Chemical shifts are reported in ppm with the residual protio solvent as an internal reference. Mass spectrometry was carried out using positive electrospray ionization on a Bruker 12 Tesla APEX-Qe FTICR-MS with an Apollo II ion source. Gas Chromatography Mass Spectrometry was performed on Agilent Technologies 5973N Mass Selective Detector coupled with Agilent 6890N Network GC System.



Scheme 2.1

Synthesis of 2-((bis(pyridin-2-ylmethyl)amino)methyl)phenol (1, L)

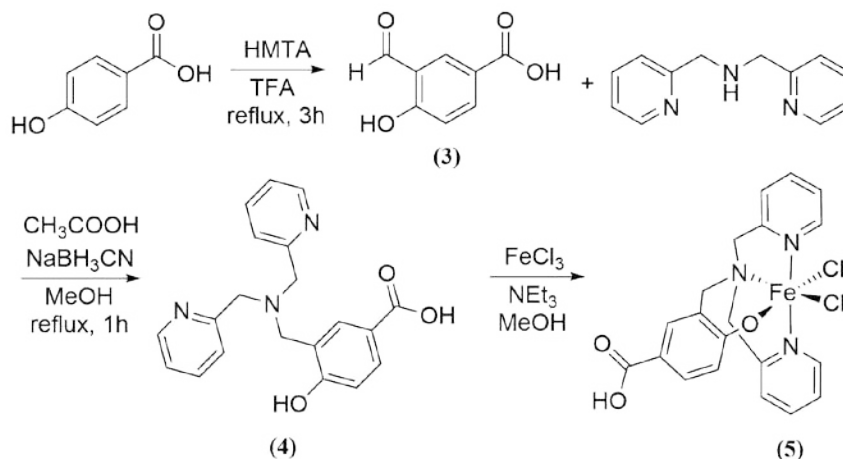
Compound **1** was synthesized using a modified literature procedure (Scheme 2.1).¹¹ To a solution of salicylaldehyde (1.00 mL, 10 mmol) in 50 mL of MeOH, a

solution of bis(pyridine-2-ylmethyl)amine (1.80 mL, 10 mmol) in 10 mL of MeOH was added. 3 drops of glacial acetic acid were added followed by the addition of a solution of sodium cyanoborohydride (0.31 g, 5 mmol) in 5 mL of MeOH. The resulting solution was allowed to reflux overnight. 1M HCl was added to the solution until it reached pH 4. The solution was evaporated to near dryness and dissolved in 60 mL of saturated NaHCO₃ solution and then extracted with DCM (3 × 60 mL). Upon removal of the volatiles, the oily residue was purified by column chromatography on silica gel. Elution with a 10% MeOH in DCM afforded the separation of a red band containing 2.32 g of **1** (54% yield). ¹H NMR (CDCl₃): 8.57 (dq, 2H), 7.63 (td, 2H), 7.35 (d, 2H), 7.17 (m, 3H), 7.07 (dd, 1H), 6.91 (dd, 1H), 6.77 (td, 1H), 3.88 (s, 4H), 3.79 (s, 2H) (Figure A1). ¹³C NMR (CDCl₃): 158.22, 157.37, 148.77, 136.81, 129.05, 123.19, 122.87, 122.19, 118.86, 116.51, 59.05, 56.93 (Figure A2).

Synthesis of [FeCl₂(L)] (**2**)

Compound **2** was synthesized using a modified literature procedure (Scheme 2.1).¹¹ To a solution of **1** (21.6 mg, 0.05 mmol) in 5 mL of MeOH, a solution of FeCl₃·6H₂O (13.5 mg, 0.05 mmol) in 5 mL of MeOH was added. The resulting mixture was left open to air and was allowed to stir at room temperature under air for 1 h. The blue solution was filtered through celite and the volatiles were removed to yield **2** as a blue solid. The product was crystalized by diffusion of diethyl ether into a concentrated solution of **2** in DCM. HRMS for

$C_{19}H_{18}ClN_3OFe^+$: predicted $m/z = 395.048233$, observed = 395.048640 (Figure A3).



Scheme 2.2

Synthesis of 3-formyl-4-hydroxybenzoic acid (3)

Compound **3** was synthesized according to the procedure reported in the literature (Scheme 2.2).¹² 4-Hydroxybenzoic acid (2.5 g, 36 mmol) and hexamethylenetetramine (HMTA) (2.5 g, 36 mmol) were stirred in 20 mL of TFA. The reaction mixture was allowed to reflux overnight. The resulting yellow solution was diluted with 100 mL of 1M HCl and extracted with diethyl ether (3 × 100 mL). The organic layer was dried with MgSO₄ and filtered. The volatiles were removed to give 1.34 g of **3** (23% yield). ¹H NMR (CD₃CN): 11.35 (br, 1H), 10.02 (d, 1H), 8.40 (dd, 1H), 7.07 (d, 1H) (Figure A4). ¹³C NMR (CD₃CN): 197.42, 165.31, 164.66, 138.80, 137.76, 136.13, 122.02, 120.37 (Figure A5).

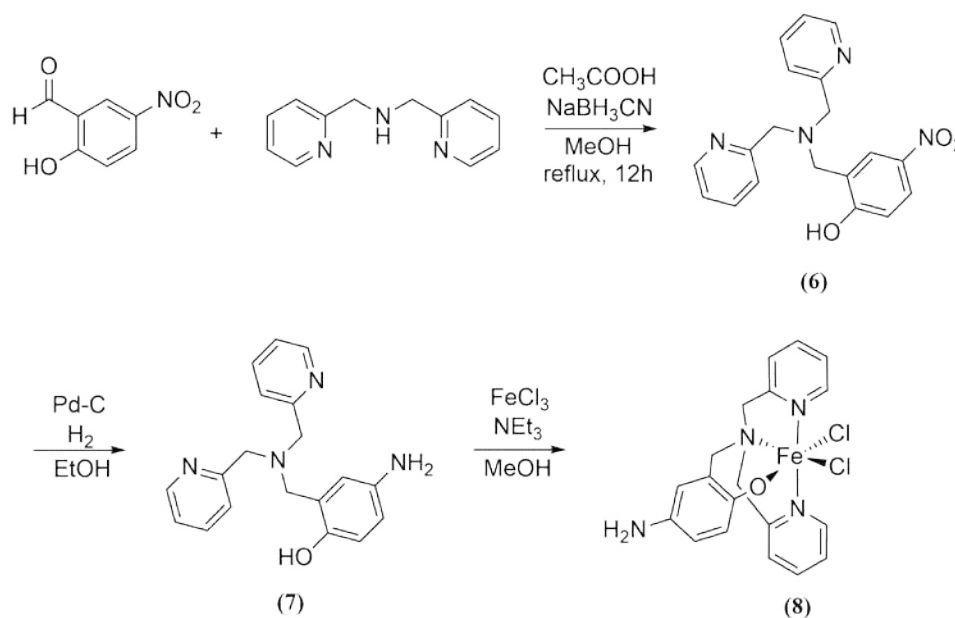
Synthesis of 3-((bis(pyridin-2-ylmethyl)amino)methyl)-4-hydroxybenzoic acid (**4**, L-COOH)

Compound **4** was synthesized using a modified literature procedure (Scheme 2.2).¹¹ To a solution of **3** (1.34 g, 8.1 mmol) in 10 mL of MeOH, a solution of bis(pyridine-2-ylmethyl)amine (1.46 mL, 8.1 mmol) in 4 mL of MeOH was added. 3 drops of glacial acetic acid were added followed by the addition of a degassed solution of sodium cyanoborohydride (0.25 g, 4.05 mmol) in 4 mL of MeOH. The resulting solution was allowed to reflux overnight. 1M HCl was added to the solution until it reached pH 4. The solution was evaporated to near dryness, dissolved in 50 mL of saturated NaHCO₃ solution and then extracted with DCM (3 × 50 mL). 1M HCl was added to the aqueous layer until it reached pH 7. The aqueous layer was extracted again with DCM (3 × 50 mL). The organic layer from the second extraction was dried with MgSO₄ and filtered. The volatiles were removed to give 0.81 g of **4** (29% yield). ¹H NMR (CDCl₃): 8.59 (m, 2H), 7.95 (dd, 1H), 7.86 (d, 1H), 7.67 (t, 2H), 7.35 (d, 2H), 7.21 (t, 2H), 6.95 (d, 1H), 3.95 (s, 4H), 3.85 (s, 2H) (Figure A6). ¹³C NMR (CDCl₃): 170.48, 162.47, 157.95, 148.31, 137.41, 131.89, 123.29, 122.50, 120.74, 116.71, 58.27, 56.76 (Figure A7). HRMS for C₂₀H₁₉N₃O₃Na⁺: predicted *m/z* = 372.131863, observed = 373.131849 (Figure A8).

Synthesis of [FeCl₂(L-COOH)] (**5**)

Compound **5** was synthesized using a modified literature procedure (Scheme 2.2).¹¹ To a solution of **4** (0.1 mg, 0.29 mmol) in 5 mL of MeOH, triethylamine

(TEA) (0.08 ml, 0.58 mmol) and a solution of $\text{FeCl}_3 \cdot 6\text{H}_2\text{O}$ (0.08 g, 0.29 mmol) in 5 mL of MeOH were added. The resulting mixture was allowed to stir under room temperature for 1 h and filtered through celite. The volatiles were removed to yield **5** as a purple solid. The product was crystallized by diffusion of diethyl ether into a concentrated solution of **5** in DCM.



Scheme 2.3

Synthesis of 2-((bis(pyridin-2-ylmethyl)amino)methyl)-4-nitrophenol (6**)**

Compound **6** was synthesized according to the procedure reported in the literature (Scheme 2.3).¹³ To a solution of 2-hydroxy-5-nitrobenzaldehyde (0.50 g, 3 mmol) in 50 mL of MeOH and a solution of bis(pyridine-2-ylmethyl)amine (0.54 mL, 3 mmol) in 5 mL of MeOH was added. 3 drops of glacial acetic acid were added followed by the addition of a degassed solution of sodium cyanoborohydride (0.18 g, 3 mmol) in 5 mL of MeOH. The resulting solution was allowed to reflux overnight. 1M HCl was added to the solution until it reached pH

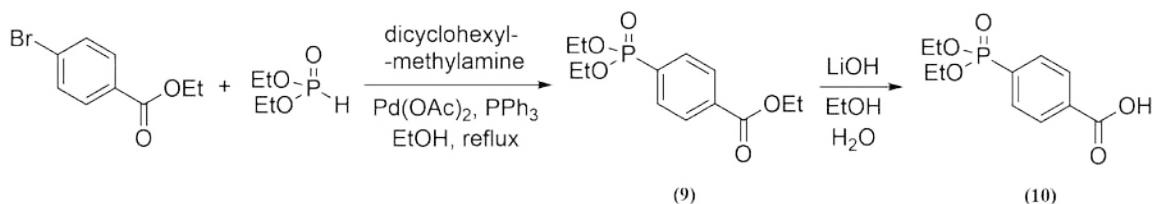
4. The solution was evaporated to near dryness, dissolved in 25 mL of saturated NaHCO₃ solution and then extracted with DCM (3 × 50 mL). The organic layer was dried with MgSO₄ and filtered. Upon removal of the volatiles, the oily residue was purified by column chromatography on silica gel. Elution with a 10% MeOH in DCM afforded the separation of a red band containing 0.83 g of **6** (79% yield). ¹H NMR (CDCl₃): 8.57 (d, 2H), 8.11 (d, 1H), 8.04 (2, 1H), 7.65 (t, 2H), 7.29 (d, 2H), 7.19 (t, 2H), 6.96 (d, 1H), 3.92 (s, 4H), 3.85 (s, 2H). (Figure A9). ¹³C NMR (CDCl₃): 164.27, 157.74, 148.69, 139.66, 137.06, 126.54, 125.61, 123.52, 123.06, 122.41, 117.14, 58.67, 56.10. (Figure A10). HRMS for C₁₉H₁₈N₄O₃H⁺: predicted m/z = 351.15, observed = 351.1.

Synthesis of 4-amino-2-((bis(pyridin-2-ylmethyl)amino)methyl)phenol (7**, L-NH₂)**

Compound **7** was synthesized using a modified literature procedure (Scheme 2.3).¹⁴ To a solution of **6** (0.83g, 2.37 mmol) in 200 mL of EtOH, palladium on activated carbon (10% Pd) (150 mg) was added. The reaction vessel was filled with hydrogen gas. The resulting mixture was allowed to stir at room temperature overnight. The light brown solution was filtered through celite and the volatiles were removed to give 0.72 g of **7** (95% yield). ¹H NMR (CDCl₃): 8.56 (m, 2H), 7.63 (dt, 2H), 7.34 (d, 2H), 7.15 (m, 2H), 6.74 (d, 1H), 6.57 (dd, 1H), 6.48 (d, 1H), 3.85 (s, 4H), 3.71 (s, 2H) (Figure A11).

Synthesis of [FeCl₂(L-NH₂)] (**8**)

Compound **8** was synthesized using a modified literature procedure (Scheme 2.3).¹¹ To a solution of **7** (0.1 mg, 0.29 mmol) in 5 mL of MeOH, TEA (0.08 mL, 0.58 mmol) and a solution of FeCl₃·6H₂O (0.08 g, 0.29 mmol) in 5 mL of MeOH were added. The resulting mixture was allowed to stir under room temperature for 1 h and filtered through celite. The volatiles were removed to yield **8** as a dark green solid. The product was crystallized by diffusion of diethyl ether in to a concentrated solution of **8** in DCM. HRMS for C₁₉H₁₉N₄OCl₂FeNa⁺: predicted *m/z* = 468.017755, observed = 468.022828 (Figure A12).



Scheme 2.4

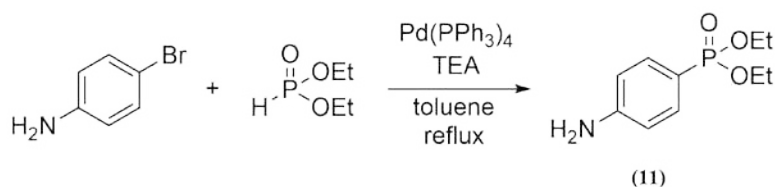
Synthesis of ethyl 4-(diethoxyphosphoryl)benzoate (**9**)

Compound **9** was synthesized according to the procedure reported in the literature (Scheme 2.4).¹⁵ To a mixture of Pd(OAc)₂ (45 mg, 0.2 mmol) and triphenylphosphine (157 mg, 0.6 mmol), a solution containing ethyl 4-bromobenzoate (2.20 mL, 18 mmol), dicyclohexylmethylamine (3.18 mL, 15 mmol) and diethyl phosphite (1.55 mL, 12 mmol) in 40 mL of EtOH was added. The resulting solution was allowed to reflux overnight. The yellow solution was diluted with 300 mL of EtOAc, and washed with 1M HCl, saturated NaHCO₃ and brine sequentially. The organic layer was dried over MgSO₄ and filtered. Upon

removal of the volatiles, the oily residue was purified by column chromatography on silica gel. Elution with a 25% hexane in EtOAc afforded the separation of a colorless band containing 2.06 g of **9** (38% yield). ^1H NMR (CDCl_3): 8.13 (m, 2H), 7.90 (m, 2H), 4.41 (dq, 2H), 4.14 (m, 4H), 1.41 (dt, 3H), 1.33 (t, 6H) (Figure A13).

Synthesis of 4-(diethoxyphosphoryl)benzoic acid (**10**)

Compound **10** was synthesized according to the procedure reported in the literature (Scheme 2.4).¹⁶ To a solution of **9** (1.70 g, 5.95 mmol) in 60 mL of MeOH, a solution of lithium hydroxide monohydrate (0.25 g, 5.95 mmol) in 60 mL of water was added dropwise. The resulting solution was allowed to stir at room temperature for 4 h. Upon removal of the volatiles, the colorless oil residue was diluted with brine and extracted with EtOAc (3 \times 80 mL). The organic layer was dried over MgSO_4 . The volatiles were removed to give 1.04 g of **10** (56% yield). ^1H NMR (CDCl_3): 8.12 (m, 2H), 7.89 (m, 2H), 4.14 (m, 4H), 1.33 (t, 6H) (Figure A14).



Scheme 2.5

Synthesis of diethyl (4-aminophenyl)phosphonate (**11**)

Compound **11** was synthesized according to the procedure reported in the literature (Scheme 2.5).¹⁷ To a mixture of 4-bromoaniline (2.76 g, 16.0 mmol) and

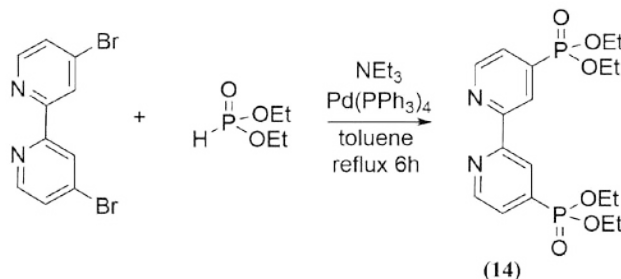
Synthesis of diethyl (4-(3-((bis(pyridin-2-ylmethyl)amino)methyl)-4-hydroxybenzamido)phenyl)phosphonate (12)

Compound **12** was synthesized using a modified literature procedure (Scheme 2.6).⁷ To a solution of **4** (0.48 g, 1 mmol) in 40 mL of anhydrous DCM, SOCl₂ (0.22 mL, 3 mmol) was added dropwise. The resulting solution was allowed to reflux for 2 h. Afterward, the volatiles were removed by bubbling Ar through the solution. A solution containing DIPEA (0.42 mL, 1.04 mmol) and **11** (0.23 g, 1 mmol) in 40 mL of anhydrous DCM were subsequently added. The resulting solution was allowed to reflux overnight. The brown solution was diluted with water (40 mL), extracted with EtOAc (3×40 mL), and washed with saturated NaHCO₃ solution (3×40 mL). The organic layer was dried with MgSO₄ and filtered. Upon removal of the volatiles, the brown solid residue was purified by column chromatography on silica gel. Elution with a 5% TEA in DCM and 10% MeOH in DCM sequentially afforded the separation of a brown band containing **12**. The product was dissolved in DCM and washed with water (3×40 mL) to remove TEA residue from the column. This afforded 0.15 g of **12** (63% yield). ¹H NMR (CDCl₃): 8.57 (dq, 2H), 7.78 (m, 4H), 7.71 (m, 2H), 7.65 (td, 2H), 7.32 (d, 2H), 7.19 (m, 2H), 6.97 (d, 1H), 4.10 (m, 4H), 3.93 (s, 4H), 3.86 (s, 2H), 1.31 (t, 6H) (Figure A18). ¹³C NMR (CDCl₃): 166.62, 161.66, 157.94, 148.30 (d, *J* = 8 Hz), 142.30 (d, *J* = 16 Hz), 136.99 (d, *J* = 12 Hz), 132.45 (d, *J* = 180 Hz), 130.34 (d, *J* = 20 Hz), 128.35 (d, *J* = 16 Hz), 124.57, 122.74 (d, *J* = 768 Hz), 123.40, 123.13, 122.35, 119.45 (d, *J* = 60 Hz), 116.91, 62.05 (d, *J* = 20 Hz), 58.82, 56.42,

16.30 (d, $J = 28$ Hz) (Figure A19). HRMS for $C_{30}H_{33}N_4O_5PH^+$: predicted $m/z = 561.226133$, observed = 561.226049 (Figure A20).

Synthesis of (4-(3-((bis(pyridin-2-ylmethyl)amino)methyl)-4-hydroxybenzamido)phenyl)phosphonic acid (**13**, $L-PO_3H_2$)

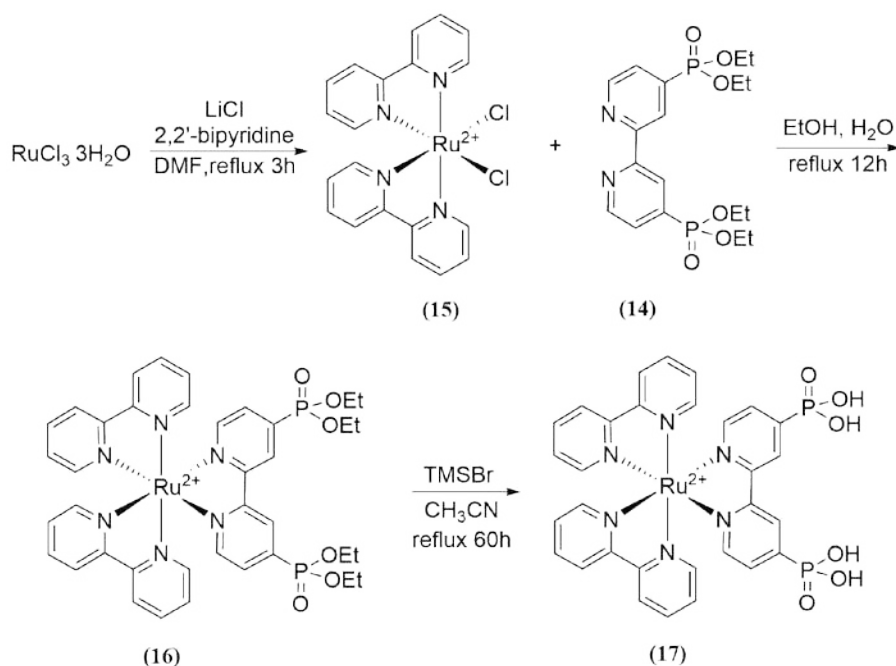
Compound **13** was synthesized using a modified literature procedure (Scheme 2.6).^{5b} To a solution of **12** (0.05 g, 0.089 mmol) in 4.5 mL of anhydrous CH_3CN , $TMSBr$ (47 μ L, 0.36 mmol) was added dropwise. The resulting solution was allowed to reflux for 60 h. The reaction was quenched with 2 mL of MeOH. The volatiles were removed to yield a brown solid. The solid was recrystallized in isopropanol to give 18 mg of **13** (42% yield). 1H NMR (CD_3OD): 8.77 (d, 2H), 8.34 (dt, 2H), 7.96 (d, 2H), 7.90 (m, 3H), 7.80 (m, 4H), 7.69 (dd, 1H), 6.74 (d, 1H), 4.52 (s, 4H), 4.06 (s, 2H) (Figure A21). ^{13}C NMR (CD_3OD): 166.40, 159.35, 152.87, 144.15, 143.08, 141.86 (d, $J = 12$ Hz), 132.23, 131.30 (d, $J = 36$ Hz), 129.94, 128.44 (d, $J = 472$ Hz), 126.00, 125.58, 125.28, 120.78, 119.90 (d, $J = 60$ Hz), 114.81, 57.16, 54.32 (Figure A22). HRMS for $C_{26}H_{25}N_4O_5PNa^+$: predicted $m/z = 505.163533$, observed = 505.163539 (Figure A23).



Scheme 2.7

Synthesis of tetraethyl 2,2'-bipyridine-4,4'-diyldiphosphonate (**14**)

Compound **14** was synthesized according to the procedure reported in literature (Scheme 2.7).^{5b} To a mixture of tetrakis(triphenylphosphite)Pd (0) (0.55 g, 0.475 mmol), 4,4'-dibromo-2,2'-bipyridine (1.5 g, 4.75 mmol), and triphenylphosphine (12.5 g, 47.5 mmol), a solution containing diethyl phosphite (1.4 mL, 10.8 mmol) and TEA (1.5 mL, 10.8 mmol) in 50 mL of toluene was added. The resulting solution was allowed to reflux for 6 h. The solution was washed with ammonium hydroxide (3×50 mL), and water (3×50 mL). The organic layer was dried over MgSO₄ and filtered. Upon removal of the volatiles, the yellow solid residue was purified by column chromatography on silica gel. Elution with a 1% MeOH in DCM and 10% MeOH in DCM sequentially afforded the separation of a colorless band containing 1.23 g of **14** (61% yield). ¹H NMR (CDCl₃): 8.84 (td, 1H), 8.77 (dt, 1H), 7.73 (dd, 1H), 4.20 (m, 4H), 1.37 (t, 6H) (Figure A24). ¹³C NMR (CDCl₃): 155.67 (d, *J* = 48 Hz), 149.58 (d, *J* = 52 Hz), 138.64 (d, *J* = 740 Hz), 125.68 (d, *J* = 36 Hz), 122.84 (d, *J* = 36), 62.79 (d, *J* = 24 Hz), 16.37 (d, *J* = 28 Hz) (Figure A25).



Scheme 2.8

Synthesis of $[\text{RuCl}_2\text{bpy}_2]$ (**15**)

Compound **15** was synthesized according to the procedure reported in literature (Scheme 2.8).^{5b} To a mixture of 2,2'-bipyridine (0.625 g, 4 mmol) and $\text{RuCl}_3 \cdot 3\text{H}_2\text{O}$ (0.523 g, 2 mmol), 25 mL of DMF was added. The resulting solution was allowed to reflux for 3 h. The solution was filtered and the residue was washed with 20 mL of 30% LiCl solution and recrystallized from ethanol to give 0.182 g of **15** (19% yield). ^1H NMR (DMSO): 9.91 (d, 2H), 8.61 (d, 2H), 8.47 (d, 2H), 8.04 (t, 2H), 7.73 (t, 2H), 7.63 (t, 2H), 7.44 (d, 2H), 7.09 (t, 2H) (Figure A26).

Synthesis of $[\text{Ru}(\text{bpy})_2(\text{tedpbpy})]\text{Cl}_2$ (**16**)

Compound **16** was synthesized according to the procedure reported in literature (Scheme 2.8).^{5b} To a mixture of **14** (88 mg, 0.21 mmol) and **15** (100 mg, 0.21 mmol), 8 mL of 1:1 EtOH: H_2O was added. The resulting solution was allowed to

reflux overnight. Upon removal of the volatiles, the residue was washed with diethyl ether to give 155 mg of **16** (81% yield). ^1H NMR (CD_3CN): 8.82 (m, 2H), 8.62 (m, 2H), 8.11 (tt, 2H), 7.93 (m, 1H), 7.71 (m, 2H), 7.63 (m, 1H), 7.43 (m, 2H), 4.20 (m, 4H), 1.34 (t, 6.03) (Figure A27).

Synthesis of $[\text{Ru}(\text{bpy})_2(\text{dpbpy})]\text{Cl}_2$ (17**, RuP)**

Compound **17** was synthesized according to the procedure reported in literature (Scheme 2.8).^{5b} To **16** (135 mg, 0.15 mmol) in 9 mL of anhydrous CH_3CN , TMSBr (0.11 mL, 0.61 mmol) was added dropwise. The resulting solution was allowed to reflux for 48 h. The reaction was quenched by adding 0.3 mL of MeOH. The resulting orange precipitate was collected by vacuum filtration and recrystallized from ethanol to give 95 mg of **17** (82% yield). ^1H NMR (D_2O): 8.59 (d, 1H), 8.36 (d, 2H), 7.87 (tt, 2H), 7.75 (m, 1H), 7.62 (m, 2H), 7.39 (m, 1H), 7.19 (t, 2H) (Figure A28).

Electrocatalytic activity studies by cyclic voltammetry

A CH Instruments 620D potentiostat with a CH Instruments 680 amp booster was used for all experiments. Each experiment was performed in a standard three-electrode cell consisting of a glassy carbon working electrode (diameter = 0.3 cm), a platinum auxiliary electrode and a SCE reference electrode. Tetrabutylammonium hexafluorophosphate (TBAPF_6 , 0.1 M) was used as the electrolyte. All electrochemical experiments were performed under an Ar atmosphere. The working and auxiliary electrodes were polished with alumina

powder paste (0.05 μm) on a cloth-covered polishing pad and then rinsed with water and acetonitrile before each scan. For the electrocatalytic activity studies, 0.5 mg of crystals of **[FeCl₂(L-NH₂)]** or **[FeCl₂(L-NH₂)]** were dissolved in 5.0 mL of 0.1 M TBAPF₆ in CH₃CN. Cyclic voltammograms (CVs) were obtained at different concentrations of trifluoroacetic acid (TFA). TFA was added till the height of the catalytic wave plateaued.

Preparation of mesoporous thin films of RuP-sensitized TiO₂

The samples for UV-vis spectroscopic measurements consist of thin mesoporous films of Degussa P25 TiO₂ nanoparticles. The nanoparticles were doctor-bladed from aqueous solution on to a glass microscope slide and annealed in a furnace at 300 °C for 2 h. The resulting slides were sensitized with **RuP** by soaking in a 0.04 mM solution of **RuP** in MeOH for 1 h. The resulting sensitized films were rinsed with MeOH and dried with a stream of Ar before analysis.

Preparation of mesoporous thin films of [FeCl₂(L-COOH)]-sensitized TiO₂

The TiO₂ slides were sensitized with **[FeCl₂(L-COOH)]** by soaking in a 0.4 mM solution of **[FeCl₂(L-COOH)]** in DCM for 1 h. The resulting sensitized films were rinsed with DCM and dried with a stream of Ar before analysis.

Preparation of mesoporous thin films of [FeCl₂(L-PO₃H₂)]-sensitized TiO₂

The TiO₂ slides were first sensitized with **L-PO₃H₂** by soaking in a 0.4 mM solution of **L-PO₃H₂** in MeOH for 1 h followed by rinsing with MeOH. Thin films

sensitized with **[FeCl₂(L-PO₃H₂)]** were prepared by soaking the films sensitized with **L-PO₃H₂** in a 0.4 mM solution of FeCl₃·6H₂O in MeOH for 1 h. The resulting sensitized films were rinsed with MeOH and dried with a stream of Ar before analysis.

Water stability studies by UV-vis spectrophotometry

Films of P25 nanoparticles were highly scattering, and spectra were obtained with an Agilent Cary 60 UV-vis spectrophotometer in conjunction with an Agilent Cary 60 Remote Diffuse Reflectance Accessory (DRA). Samples of **[FeCl₂(L-COOH)]-TiO₂** and **[FeCl₂(L-PO₃H₂)]-TiO₂** were co-sensitized with **RuP** by soaking the films in a 0.04 mM solution of **RuP** in MeOH for 1 h. The resulting sensitized films were rinsed with MeOH and dried with a stream of Ar before recording the spectra. For water stability studies, **RuP/[FeCl₂(L-COOH)]** and **RuP/[FeCl₂(L-PO₃H₂)]** sensitized TiO₂ thin films were submerged in deionized water for 1 h. Once removed from the water solution, the slides were rinsed with additional deionized water and dried under a stream of Ar for 5 min before recording the spectra.

Results and Discussion

Catalytic activity study of $[\text{FeCl}_2(\text{L-COOH})]$ and $[\text{FeCl}_2(\text{L-NH}_2)]$

Previously, we have reported $[\text{FeCl}_2(\text{L})]$ as an active catalyst for proton reduction under aqueous conditions.¹¹ To incorporate the catalyst into a TiO_2 -based AP system, we synthesized $[\text{FeCl}_2(\text{L-COOH})]$ (Scheme 2.2) and $[\text{FeCl}_2(\text{L-NH}_2)]$ (Scheme 2.3). Before sensitizing TiO_2 with the iron complexes, it is of interest to evaluate their usefulness as electrocatalysts for proton reduction.

Cyclic voltammetry (CV) is a common employed experimental method of assessing the activity of catalysts for proton reduction. This technique helps elucidate catalytic mechanisms and show the electrochemical response of a catalyst upon addition of a weak acid (e.g. trifluoroacetic acid) as the proton source. The appearance of an irreversible catalytic wave indicates that the catalyst is capable of proton reduction.¹⁸ The ratio of the current at the top of the irreversible catalytic wave (i_c), and the current at the reversible reduction of the catalyst in the absence of acid (i_p) provides an estimation of catalytic activity. A large i_c/i_p , indicates that the catalyst can achieve a high turnover frequency (TOF) for the electrocatalytic reduction of protons to hydrogen gas.¹⁹

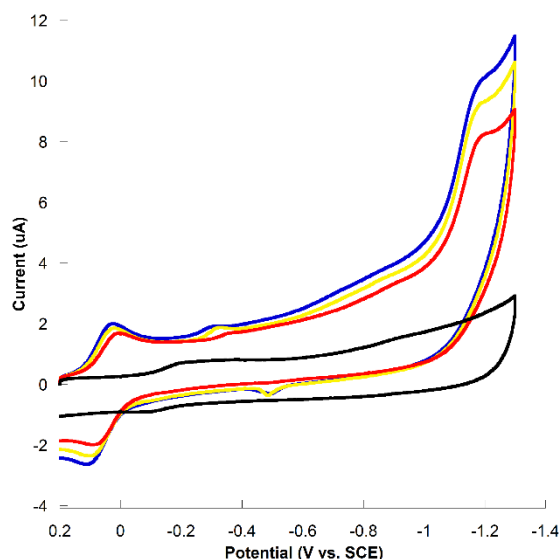


Figure 2.3. Cyclic Voltammograms of **[FeCl₂(L-COOH)]** in CH₃CN solution with 0.1 M TBAPF₆ at a scan rate of 200 mV/s without acid added (black) and upon the addition of 11 mM (red), 22 mM (yellow), 33 mM (blue) TFA.

The CVs of **[FeCl₂(L-COOH)]** show a reversible reduction of Fe^{III} to Fe^{II} at -0.23 V vs. SCE in the absence of trifluoroacetic acid (TFA). Upon addition of 1.1 mM of TFA, the redox couple shifts to 0.03 V vs. SCE, and an irreversible catalytic wave occurs at -1.19 V vs. SCE. As increasing amount of TFA is added to the solution, the current of the catalytic wave increases, resulting a final i_c/i_p of 5.64 (Figure 2.3).

The i_c/i_p of **[FeCl₂(L-COOH)]** is lower than that of the parent complex **[FeCl₂(L)]**. However, the catalytic events of **[FeCl₂(L-COOH)]** and the **[FeCl₂(L)]** are observed at very similar potential (-1.19 V vs. SCE and -1.17 V vs. SCE). It must also be noted that the cathodic shift of the Fe³⁺/Fe²⁺ redox couple upon acid addition is observed in the CVs of **[FeCl₂(L)]** as well. This indicates that the oxygen of the phenolate in **[FeCl₂(L-COOH)]** is most likely protonated followed by the reduction of Fe^{III} to Fe^{II} and the catalysis event, suggesting a CEEC or a

CECE mechanism.¹¹ Therefore, although making the iron complex less active than **[FeCl₂(L)]**, functionalizing the ligand with a carboxylate anchoring group does not affect the potential of the catalytic event or the mechanism of the catalyst.

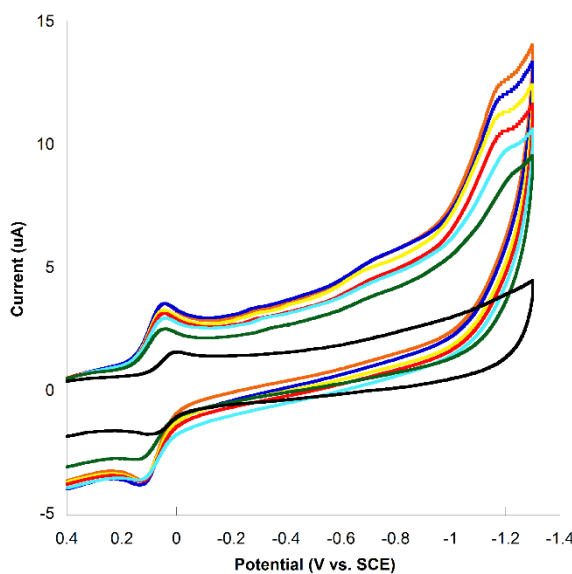


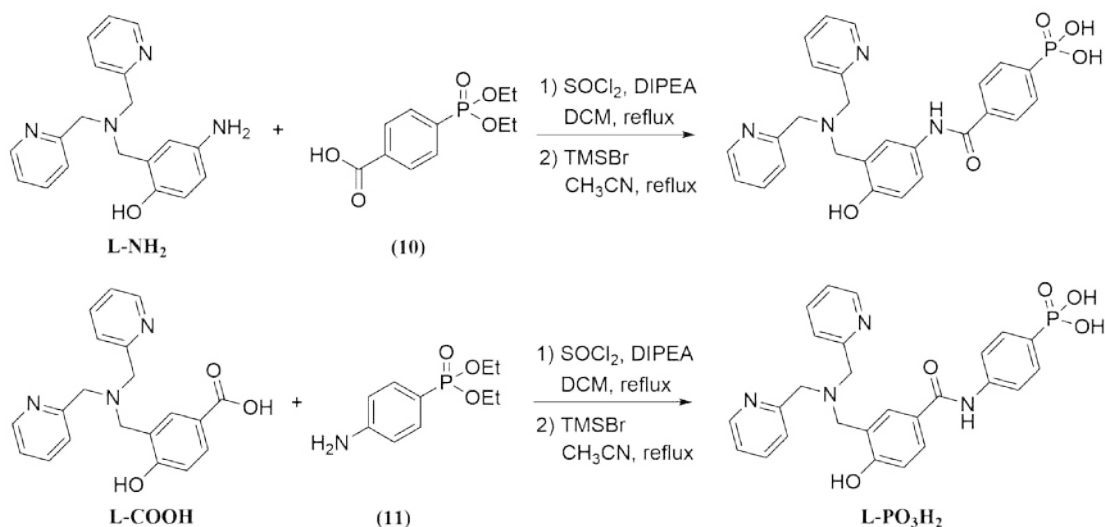
Figure 2.4. Cyclic Voltammograms of **[FeCl₂(L-NH₂)]** in a CH₃CN solution with 0.1 M TBAPF₆ at a scan rate of 200 mV/s without acid added (black) and upon the addition of 11 mM (green), 22 mM (blue), 33 mM (red), 44 mM (yellow), 55 mM (purple), 66 mM (orange) TFA.

The CVs of **[FeCl₂(L-NH₂)]** show a reversible reduction of Fe^{III} to Fe^{II} at 0 V vs. SCE in the absence of TFA. Upon addition of 1.1 mM of TFA, the reversible reduction shifts to 0.03 V vs. SCE, and an irreversible catalytic wave occurs at -1.17 V vs. SCE. As increasing amount of TFA is added to the solution, a larger current enhancement is observed, resulting a final i_c/i_p of 8.18 (Figure 2.4).

Similar to **[FeCl₂(L-COOH)]**, the cathodic shift of the Fe³⁺/Fe²⁺ redox couple in the CVs of **[FeCl₂(L-NH₂)]** suggests a CEEC or a CECE mechanism. The catalytic event is observed at the same potential as the parent complex

[FeCl₂(L)]. Interestingly, functionalizing the ligand with amine does not affect the catalytic activity of the complex. The i_a/i_p of **[FeCl₂(L-COOH)]** compares favorably with **[FeCl₂(L)]** that produces $i_a/i_p = 7.8$ under the same experimental condition.

Immobilization of the iron catalyst on TiO₂ via a phosphonate anchoring group

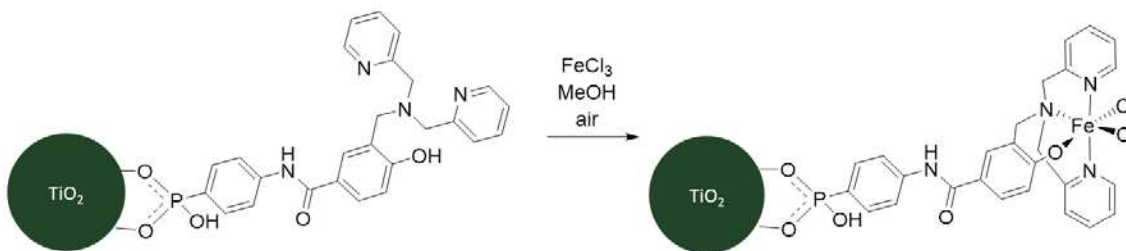


Scheme 2.9. Attempted syntheses to functionalize the ligand with phosphonate anchoring group.

After the electrochemical studies establishing both **[FeCl₂(L-NH₂)]** and **[FeCl₂(L-COOH)]** as active catalysts for hydrogen evolution, attempts were made to immobilize the complexes on TiO₂ via phosphonate anchoring groups by coupling **L-NH₂** and **L-COOH** to molecular phosphonate linkers (**10**, **11**) (Scheme 2.9). However, the coupling between **L-NH₂** and **10** failed as only the starting materials were shown in ¹H NMR spectrum. The unsuccessful coupling reaction is most likely a result of quick **L-NH₂** decomposition. Additionally, the 1° amine

might not be nucleophilic enough to attack the acid chloride to initiate the reaction.

The coupling of **L-COOH** to **11** successfully yielded ligand **L-PO₃H₂** with a phosphonate anchoring group (Scheme 2.9). However, **[FeCl₂(L-PO₃H₂)]** could not be synthesized from a direct complexation reaction between **L-PO₃H₂** and FeCl₃·H₂O because the unprotected phosphonic acid functional group can chelate to the iron center to form an insoluble polymer. An alternative approach is to protect the phosphonic acid with ethyl groups before performing complexation reaction. Although this synthetic route can avoid the formation of polymer, the following deprotection reaction ultimately leads to decomposition of the iron complex.



Scheme 2.10. Loading TiO₂ films with **[FeCl₂(L-PO₃H₂)]**.

A simple solution to this problem is to first immobilize **L-PO₃H₂** on TiO₂, then complex the ligand to FeCl₃·H₂O on the surface of TiO₂ (Scheme 2.10). Since TiO₂ can form strong covalent bonds with phosphonic acid, it acts as a protective group to prevent chelation of phosphonic acid to iron. However, there are two prerequisites for this procedure: (1) the ligand can complex to FeCl₃·H₂O under air; (2) complexation can take place without the presence of triethylamine (TEA). The purpose of TEA is to deprotonate the hydroxyl group on the ligand. But since adsorption of TEA on TiO₂ surface can complicate the analysis of

[FeCl₂(L-PO₃H₂)] that has been immobilized on TiO₂, performing the reaction without TEA is preferred.

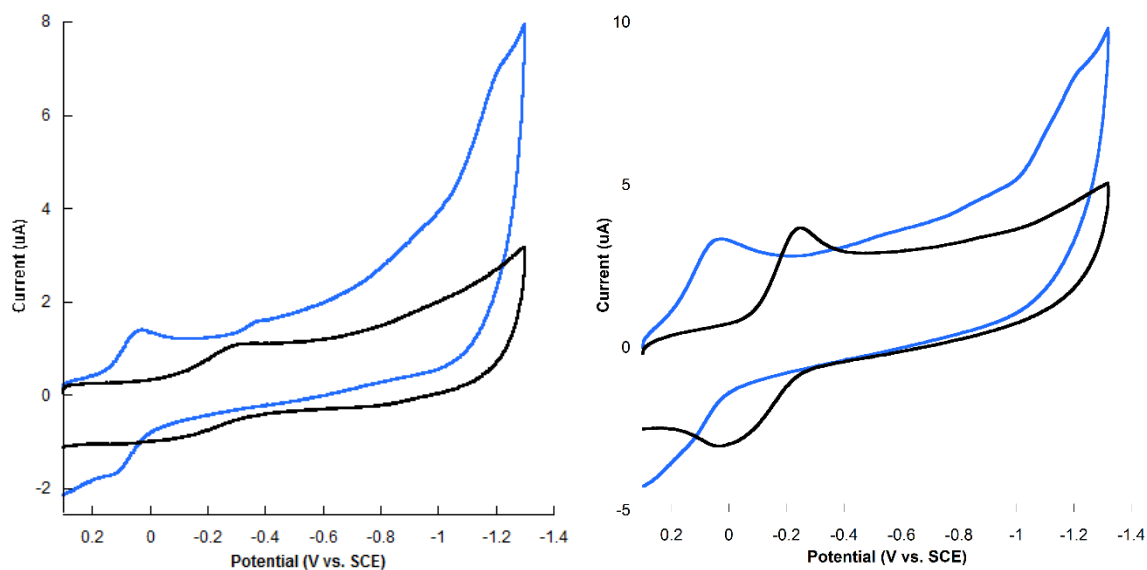


Figure 2.5. Cyclic Voltammograms of **[FeCl₂(L)]** in a CH₃CN solution with 0.1 M TBAPF₆ at a scan rate of 200 mV/s without acid added (black) and upon the addition of 11 mM (blue) TFA. *Left:* The complex was synthesized under air without TEA. *Right:* The complex was synthesized under Ar with TEA.

To prove that **[FeCl₂(L)]** can be synthesized under air in the absence of TEA, the parent catalyst **[FeCl₂(L)]** was synthesized by mixing **L** and FeCl₃·H₂O in methanol under air (Scheme 2.1). Figure 2.5 *Left* shows the CVs of the reaction product. In the absence of TFA, there is a reversible reduction at 0.27 V vs. SCE. Upon addition of 1.1 M TFA to the solution, the reversible reduction shifts to 0.02 V vs. SCE, and an irreversible reduction event occurs at -1.19 V vs. SCE. The potentials of the redox couple and the catalytic events for are consistent with those of **[FeCl₂(L)]** (Figure 2.5 *Right*). Therefore, **[FeCl₂(L-PO₃H₂)]** can be synthesized on the surface of TiO₂ under air without TEA.

Stability studies of the anchoring groups under aqueous conditions

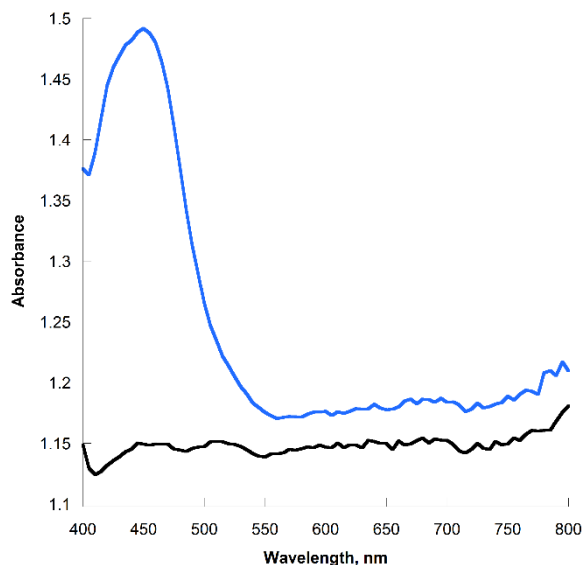


Figure 2.6. UV-vis of TiO₂ thin film (black), and covalently attached **RuP** (blue).

Photosensitizer **RuP** was synthesized by modifying a literature procedure (Scheme 2.8). A TiO₂ film was sensitized with **RuP** and the loading of the photosensitizer on TiO₂ was monitored using UV-vis spectroscopy. While a clean TiO₂ thin film is white, the **RuP**-sensitized TiO₂ thin film appears to be orange, suggesting that the dye-sensitization extends the absorption edge of pure TiO₂ from UV to visible-light region.²⁰ The UV/vis spectra of pure and **RuP**-sensitized TiO₂ thin films are shown in Figure 2.6. The spectra confirm that the pure Degussa P25 TiO₂ nanoparticles used in this study do not absorb much visible light as predicted from the 3.2 eV band gap. **RuP**-sensitized TiO₂ exhibits a strong absorption band from 375 nm to 700 nm with λ_{max} at 450 nm (Figure 2.6)

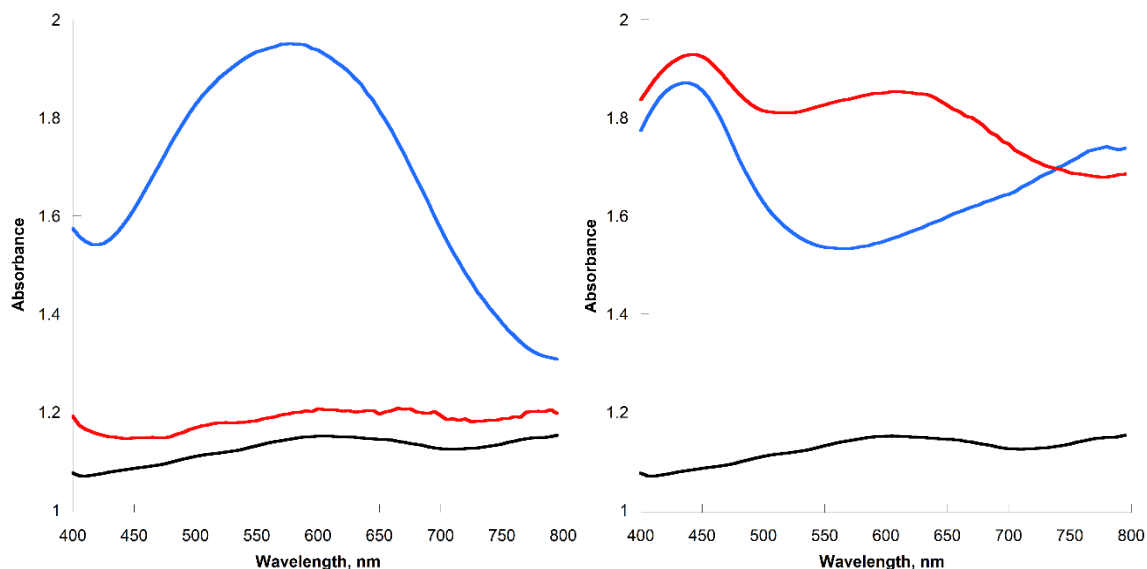


Figure 2.7. *Left:* UV-vis of TiO₂ thin film (black) with [FeCl₂(L)] (red), and covalently attached [FeCl₂(L-COOH)] (blue). *Right:* UV/VIS of TiO₂ thin film (black) co-sensitized with RuP and [FeCl₂(L-COOH)] before exposure to water (red), and after exposure to water (blue).

that corresponds to the metal-to-ligand charge transfer (MLCT) transition. The absorption wavelength is consistent with that reported previously.^{5a}

TiO₂ films were sensitized with [FeCl₂(L-COOH)] in dichloromethane (DCM) and catalyst loading was monitored using UV-vis spectroscopy. The UV-vis spectrum is compared to the spectrum of a TiO₂ film incubated in DCM containing the parent complex [FeCl₂(L)]. As shown in Figure 2.7 *Left*, [FeCl₂(L-COOH)]-sensitized TiO₂ film exhibits a broad absorption band from 425 nm to 750 nm with λ_{max} at 605 nm. In contrast, the spectrum of the TiO₂ film in [FeCl₂(L)] solution has almost no absorption in the visible light region. This suggests that the carboxyl functional group can covalently immobilize the catalyst on TiO₂ under non-aqueous condition.

To assess the stability of the covalent attachment between the carboxylate anchoring group and TiO₂ under aqueous condition, we co-sensitized a TiO₂ film

with **RuP** and **[FeCl₂(L-COOH)]**, then incubated the film in deionized water for 1 h. Figure 2.7 *Right* shows the UV-vis spectra of the co-sensitized TiO₂ film before and after exposure to water. Before exposure to water, the TiO₂ film exhibits two absorption band with λ_{max} at 450 nm (**RuP**) and 605 nm (**[FeCl₂(L-COOH)]**). After incubation in water, a large decrease in the absorbance at 605 nm is observed for **[FeCl₂(L-COOH)]** attached through the carboxylic acid. This decrease in absorbance indicates a significant desorption of **[FeCl₂(L-COOH)]** from the TiO₂ surface, suggesting a hydrolysis of the covalent bond between the carboxylic acid and TiO₂ under aqueous condition.

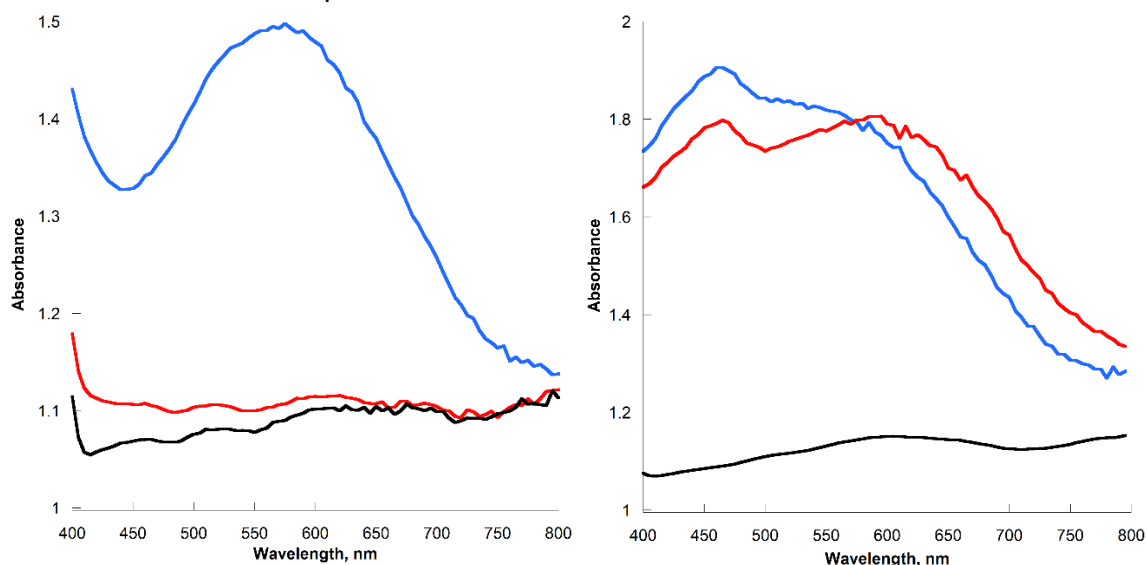


Figure 2.8. *Left:* UV-vis of TiO₂ thin film (black) with FeCO₃I₃·H₂O (red), and covalently attached **[FeCl₂(L-PO₃H₂)]** (blue). *Right:* UV-vis of TiO₂ thin film (black) co-sensitized with **RuP** and **[FeCl₂(L-PO₃H₂)]** before exposure to water (red), and after exposure to water (blue).

A TiO₂ films was sensitized with **[FeCl₂(L-PO₃H₂)]** using the method established in the previous section. The loading of the catalyst was monitored using UV-vis spectroscopy. The UV-vis spectrum is compared to the spectrum of a TiO₂ film incubated in methanol containing FeCl₃·H₂O. As shown in Figure 2.8 *Left*, **[FeCl₂(L-PO₃H₂)]**-sensitized TiO₂ film exhibits a broad absorption band from

440 nm to 800 nm with λ_{\max} at 575 nm. In contrast, the spectrum of the TiO_2 film in $\text{FeCl}_3 \cdot \text{H}_2\text{O}$ solution has almost no absorption in the visible light region. This suggests that the **L-PO₃H₂** has been successfully complexed to $\text{FeCl}_3 \cdot \text{H}_2\text{O}$ on the surface of TiO_2 .

To assess the stability of the covalent attachment between the phosphonate anchoring group and TiO_2 under aqueous condition, we co-sensitized a TiO_2 film with **RuP** and **[FeCl₂(L-PO₃H₂)]**, then incubated the film in deionized water for 1 h. Figure 2.8 *Right* shows the UV-vis spectra of the co-sensitized TiO_2 film before and after exposure to water. Before exposure to water, the TiO_2 film exhibits two absorption band with λ_{\max} at 450 nm (**RuP**) and 575 nm (**[FeCl₂(L-PO₃H₂)]**). After incubation in water, only a small decrease in the absorbance at 575 nm is observed for **[FeCl₂(L-PO₃H₂)]** immobilized via phosphonic acid. In comparison to carboxylic acid anchor (Figure 2.6), it is apparent that the bonding between the phosphonate anchor of **[FeCl₂(L-PO₃H₂)]** and TiO_2 is more stable under aqueous condition.

Conclusion

The electrochemistry results of **[FeCl₂(L-COOH)]** and **[FeCl₂(L-NH₂)]**, and the UV-vis studies of TiO₂ thin films sensitized with **RuP**, **[FeCl₂(L-COOH)]**, and **[FeCl₂(L-PO₃H₂)]** are presented. Electrochemical studies established that **[FeCl₂(L-COOH)]** has an i_o/i_p of 5.64, and **[FeCl₂(L-NH₂)]** has an i_o/i_p of 8.18. The two iron complexes are therefore both catalytically active for hydrogen generation. However, the attempts to couple **[FeCl₂(L-NH₂)]** to the phosphonate molecular linker failed. Thus, **[FeCl₂(L-PO₃H₂)]** was synthesized by coupling **[FeCl₂(L-COOH)]** and the molecular phosphonate linker **11**. UV-vis study of TiO₂ thin film co-sensitized with **RuP** and **[FeCl₂(L-COOH)]** shows that the carboxylate anchoring group undergoes considerable hydrolysis after exposure to water. In contrast, the phosphonate anchoring group of **[FeCl₂(L-PO₃H₂)]** exhibits robust attachment under aqueous conditions. Since the hydrogen evolution experiments are carried out in aqueous environment, **[FeCl₂(L-PO₃H₂)]** is a more suitable catalyst for the TiO₂-based photocatalytic system.

References

1. (a) Lakadamyali, F.; Reisner, E., Photocatalytic H₂ Evolution from Neutral Water with a Molecular Cobalt Catalyst on a Dye-Sensitized TiO₂ Nanoparticle. *Chem. Commun.* **2011**, 47 (6), 1695-1697; (b) Youngblood, W. J.; Lee, S.-H. A.; Kobayashi, Y.; Hernandez-Pagan, E. A.; Hoertz, P. G.; Moore, T. A.; Moore, A. L.; Gust, D.; Mallouk, T. E., Photoassisted Overall Water Splitting in a Visible Light-Absorbing Dye-Sensitized Photoelectrochemical Cell. *J. Am. Chem. Soc.* **2009**, 131 (3), 926-927.
2. Brennan, B. J.; Llansola Portoles, M. J.; Liddell, P. A.; Moore, T. A.; Moore, A. L.; Gust, D., Comparison of Silatrane, Phosphonic Acid, and Carboxylic Acid Functional Groups for Attachment of Porphyrin Sensitizers to TiO₂ in Photoelectrochemical Cells. *Physical Chemistry Chemical Physics* **2013**, 15 (39), 16605-16614.
3. (a) McNamara, W. R.; Milot, R. L.; Song, H.; Snoeberger Iii, R. C.; Batista, V. S.; Schmuttenmaer, C. A.; Brudvig, G. W.; Crabtree, R. H., Water-Stable, Hydroxamate Anchors for Functionalization of TiO₂ Surfaces with Ultrafast Interfacial Electron Transfer. *Energy & Environmental Science* **2010**, 3 (7), 917-923; (b) Rozhkova, E. A., and Ariga, K., *From Molecules to Materials: Pathways to Artificial Photosynthesis*. Springer: 2015.
4. Nazeeruddin, M. K.; Kay, A.; Rodicio, I.; Humphry-Baker, R.; Mueller, E.; Liska, P.; Vlachopoulos, N.; Graetzel, M., Conversion of Light to Electricity by cis-X₂Bis(2,2'-Bipyridyl-4,4'-Dicarboxylate)Ruthenium(II) Charge-Transfer Sensitizers (X = Cl⁻, Br⁻, I⁻, CN⁻, and SCN⁻) on Nanocrystalline Titanium Dioxide Electrodes. *J. Am. Chem. Soc.* **1993**, 115 (14), 6382-6390.
5. (a) Lakadamyali, F.; Reynal, A.; Kato, M.; Durrant, J. R.; Reisner, E., Electron Transfer in Dye-Sensitized Semiconductors Modified with Molecular Cobalt Catalysts: Photoreduction of Aqueous Protons. *Chem. Eur. J.* **2012**, 18 (48), 15464-15475, S15464/1-S15464/18; (b) Neuthe, K., Phosphonic Acid Anchored Ruthenium Complexes for ZnO-Based Dye-Sensitized Solar Cells. *Dyes and pigments* **2014**, 104, 24-33.
6. Han, Z.; Qiu, F.; Eisenberg, R.; Holland, P. L.; Krauss, T. D., Robust Photogeneration of H₂ in Water Using Semiconductor Nanocrystals and a Nickel Catalyst. *Science* **2012**, 338 (6112), 1321-1324.
7. McNamara, W. R.; Snoeberger, R. C.; Li, G.; Schleicher, J. M.; Cady, C. W.; Poyatos, M.; Schmuttenmaer, C. A.; Crabtree, R. H.; Brudvig, G. W.; Batista, V. S., Acetylacetonate Anchors for Robust Functionalization of TiO₂ Nanoparticles with Mn(II)-Terpyridine Complexes. *J. Am. Chem. Soc.* **2008**, 130 (43), 14329-14338.
8. Thomas, A. G.; Syres, K. L., Adsorption of Organic Molecules on Rutile TiO₂ and Anatase TiO₂ Single Crystal Surfaces. *Chemical Society Reviews* **2012**, 41 (11), 4207-4217.
9. Nazeeruddin, M. K.; Humphry-Baker, R.; Liska, P.; Grätzel, M., Investigation of Sensitizer Adsorption and the Influence of Protons on Current and Voltage

- of a Dye-Sensitized Nanocrystalline TiO₂ Solar Cell. *J. Phys. Chem. B* **2003**, *107* (34), 8981-8987.
10. Bae, E.; Choi, W.; Park, J.; Shin, H. S.; Kim, S. B.; Lee, J. S., Effects of Surface Anchoring Groups (Carboxylate vs Phosphonate) in Ruthenium-Complex-Sensitized TiO₂ on Visible Light Reactivity in Aqueous Suspensions. *J. Phys. Chem. B* **2004**, *108* (37), 14093-14101.
 11. Connor, G. P.; Mayer, K. J.; Tribble, C. S.; McNamara, W. R., Hydrogen Evolution Catalyzed by an Iron Polypyridyl Complex in Aqueous Solutions. *Inorganic Chemistry* **2014**, *53* (11), 5408-5410.
 12. Talukdar, D.; Panda, S.; Borah, R.; Manna, D., Membrane Interaction and Protein Kinase C-C1 Domain Binding Properties of 4-Hydroxy-3-(hydroxymethyl) Phenyl Ester Analogues. *J. Phys. Chem. B* **2014**, *118* (27), 7541-7553.
 13. Hartley, C. L.; DiRisio, R. J.; Chang, T. Y.; Zhang, W.; McNamara, W. R., Electrocatalytic Hydrogen Evolution by an Iron Complex Containing a Nitro-Functionalized Polypyridyl Ligand. *Polyhedron* **2016**, *114*, 133-137.
 14. Vanier, G. S.; Vanier, G. S., Simple and Efficient Microwave-Assisted Hydrogenation Reactions at Moderate Temperature and Pressure. *ChemInform* **2007**, *38* (19).
 15. Goossen, L. J.; Goossen, L. J.; Dezfuli, M. K., Practical Protocol for the Palladium-Catalyzed Synthesis of Arylphosphonates from Bromoarenes and Diethyl Phosphite. *ChemInform* **2005**, *36* (29).
 16. Metcalf, C. A., III; Shakespeare, W. C.; Sawyer, T. K.; Wang, Y.; Bohacek, R. Preparation of Phosphorus-Substituted Pyridopyrimidones as Therapeutic Agents. WO2003000270A1, 2003.
 17. Kim, Y.-C.; Brown, S. G.; Harden, T. K.; Boyer, J. L.; Dubyak, G.; King, B. F.; Burnstock, G.; Jacobson, K. A., Structure-Activity Relationships of Pyridoxal Phosphate Derivatives as Potent and Selective Antagonists of P2X₁ Receptors. *Journal of Medicinal Chemistry* **2001**, *44* (3), 340-349.
 18. Fourmond, V.; Jacques, P.-A.; Fontecave, M.; Artero, V., H₂ Evolution and Molecular Electrocatalysts: Determination of Overpotentials and Effect of Homoconjugation. *Inorganic Chemistry* **2010**, *49* (22), 10338-10347.
 19. Eckenhoff, W. T.; McNamara, W. R.; Du, P.; Eisenberg, R., Cobalt Complexes as Artificial Hydrogenases for the Reductive Side of Water Splitting. *Biochimica et Biophysica Acta (BBA) - Bioenergetics* **2013**, *1827* (8-9), 958-973.
 20. Durrell, A. C.; Li, G.; Koepf, M.; Young, K. J.; Negre, C. F. A.; Allen, L. J.; McNamara, W. R.; Song, H.; Batista, V. S.; Crabtree, R. H.; Brudvig, G. W., Photoelectrochemical Oxidation of a Turn-on Fluorescent Probe Mediated by a Surface Mn^{II} Catalyst Covalently Attached to TiO₂ Nanoparticles. *Journal of Catalysis* **2014**, *310*, 37-44.

Appendix A

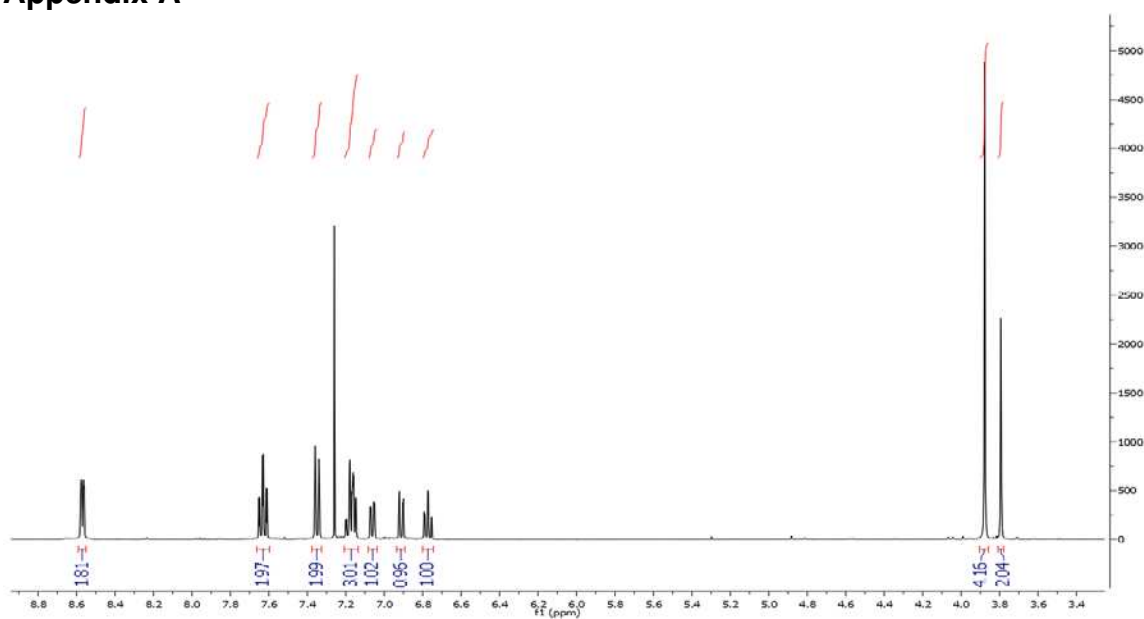
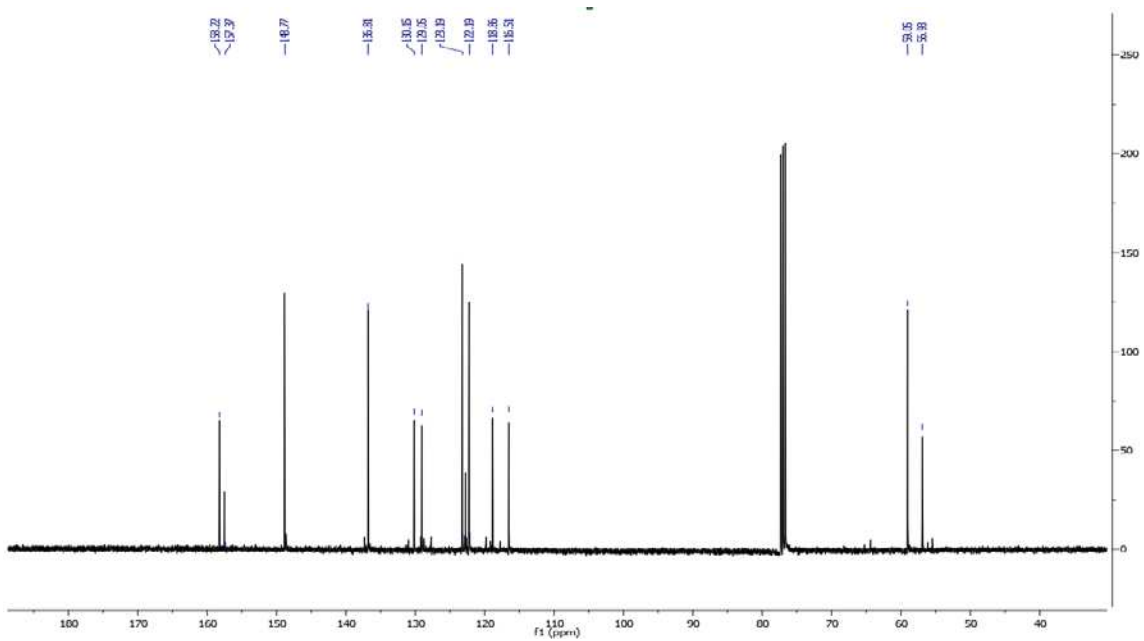


Figure A1. ^1H NMR spectrum of **1** with integrations in blue.



FigureA2. ^{13}C NMR spectrum of **1**.

Sample name: WRM01

Exact mass of $\text{C}_{19}\text{H}_{18}\text{ClN}_3\text{OFe}^+$ = 395.048233 m/z

Exact mass observed = 395.048640 m/z

Difference = < 1.0 ppm

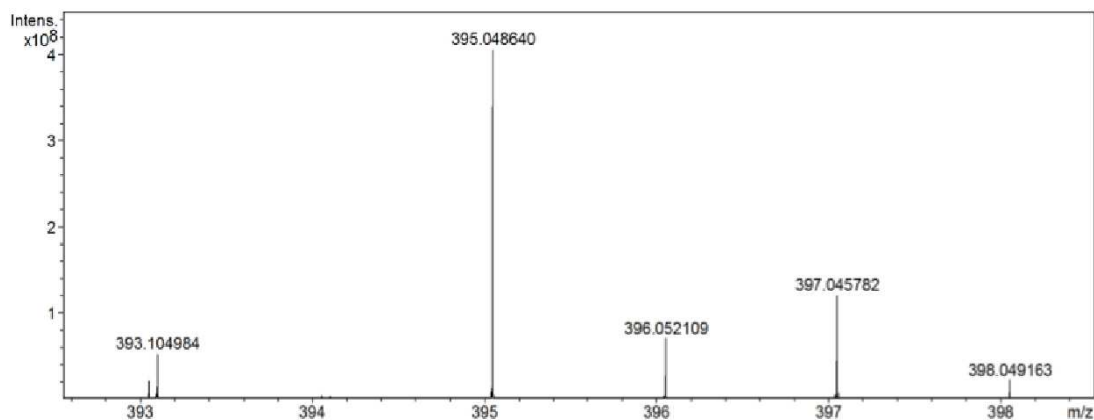


Figure A3. High-resolution mass spectrum of **2** in 1:1 THF:MeOH w/ NaCl. The expected molecular ions were observed with a difference of less than 1 ppm.

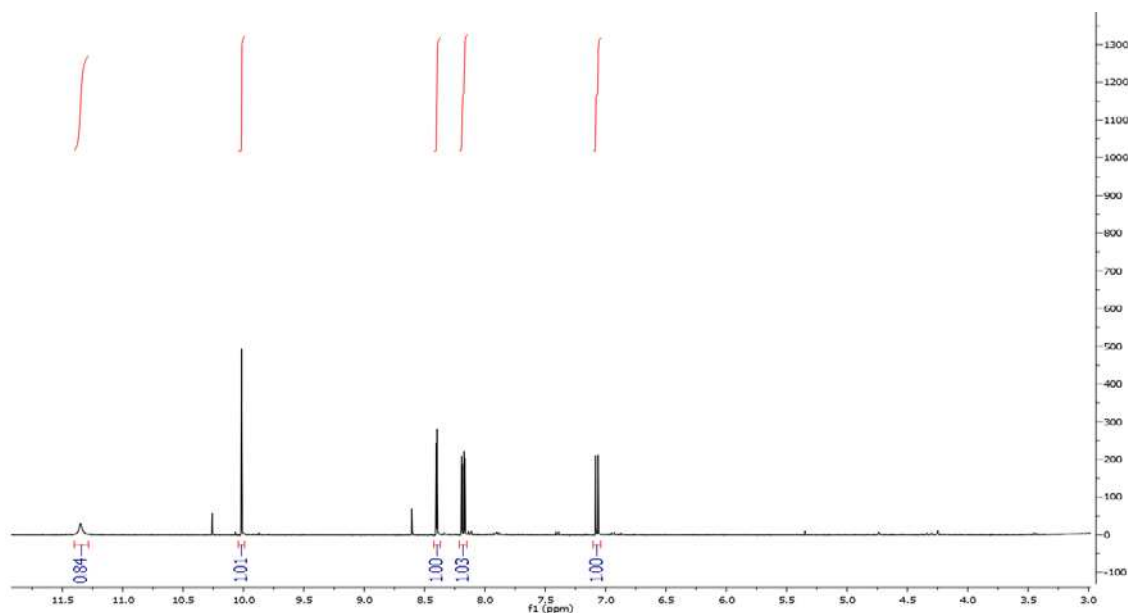


Figure A4. ¹H NMR spectrum of **3** with integrations in blue.

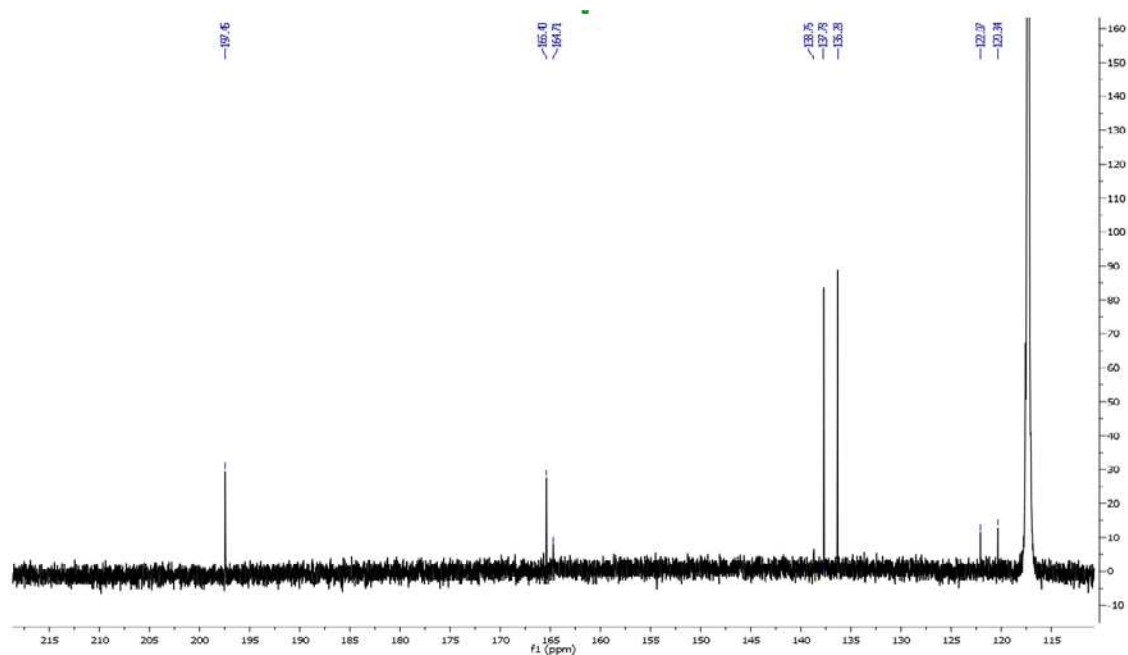


Figure A5. ^{13}C NMR spectrum of **3**.

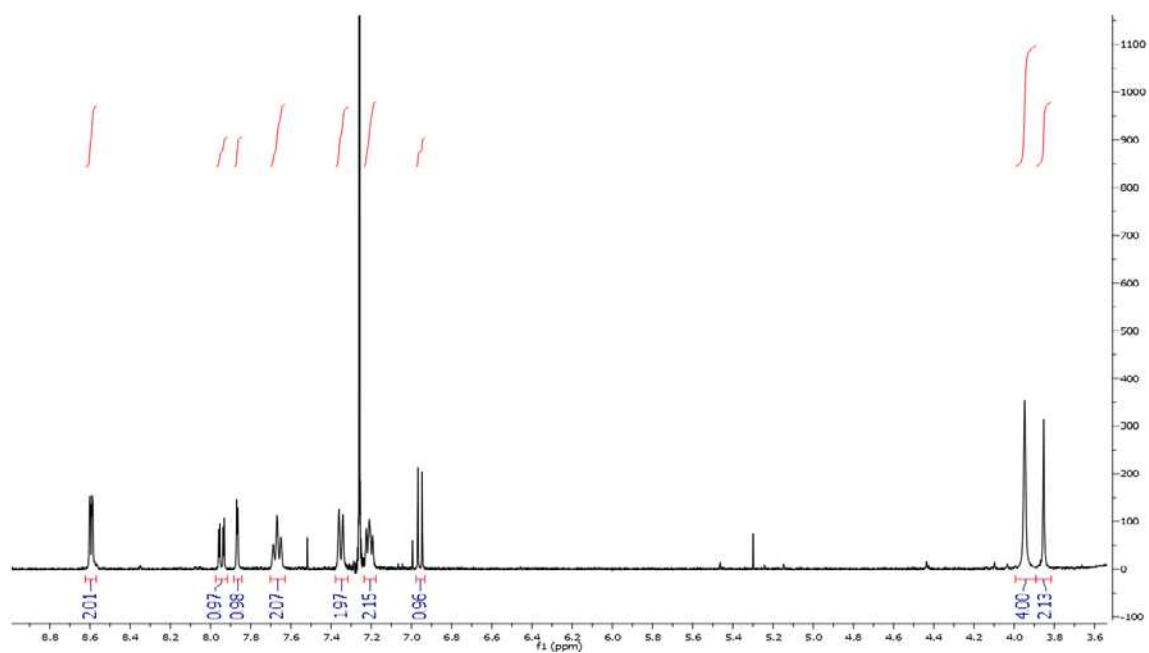


Figure A6. ^1H NMR spectrum of **4** with integrations in blue.

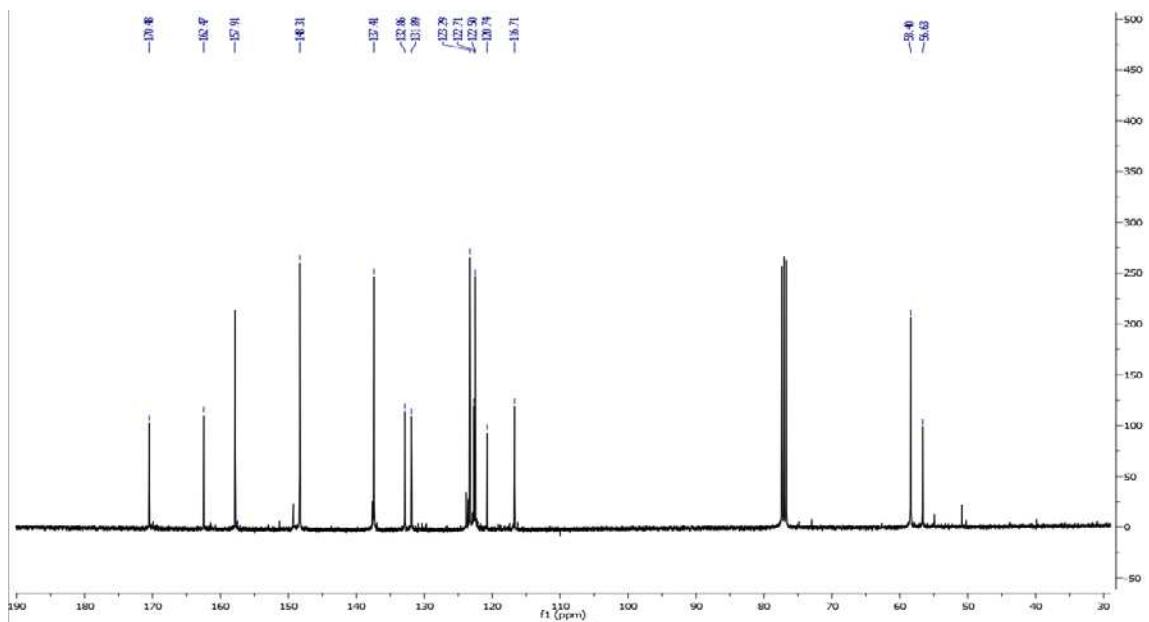


Figure A7. ^{13}C NMR spectrum of **4**.

Sample Name: WRM013

Exact Mass of $\text{C}_{20}\text{H}_{19}\text{N}_3\text{O}_3\text{Na}^+$ = 372.131863 u

Observed Mass = 372.131849 u

Difference = < 1.0 ppm

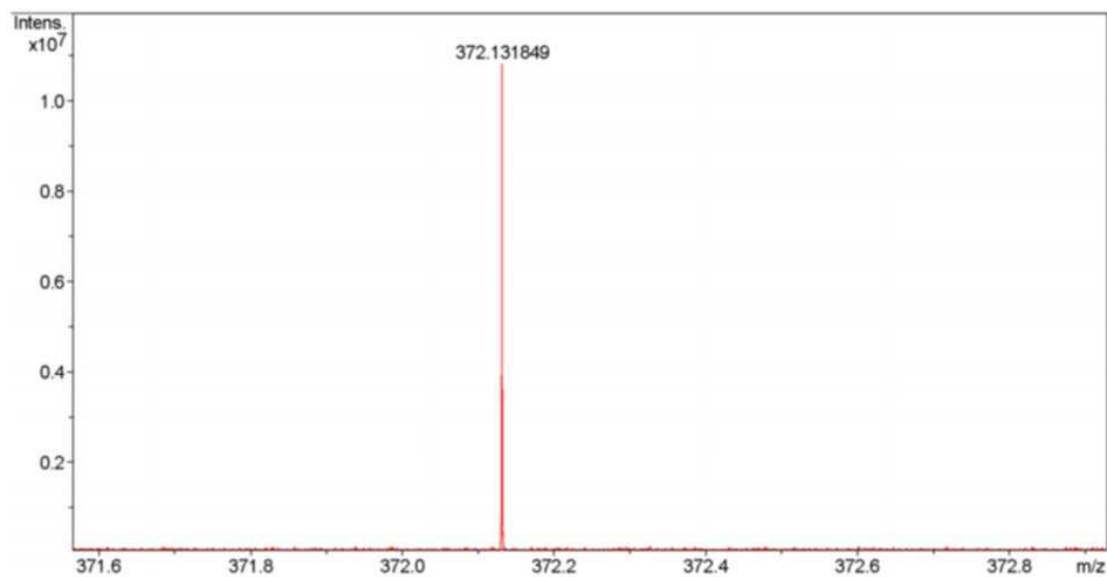


Figure A8. High-resolution mass spectrum of **4** in 1:1 THF:MeOH w/ NaCl. The expected molecular ions were observed with a difference of less than 1 ppm.

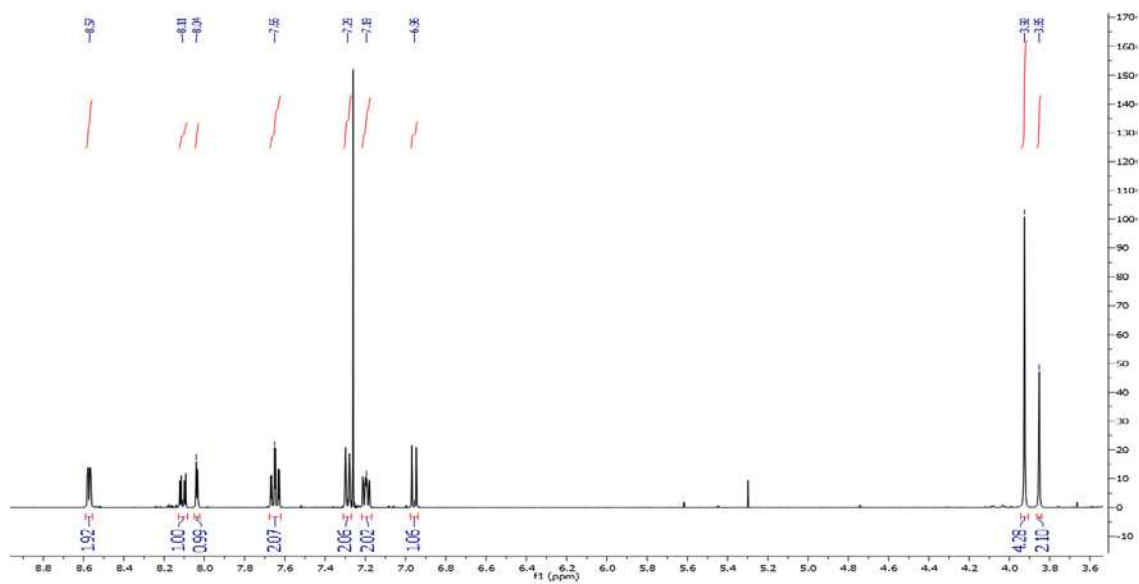


Figure A9. ¹H NMR spectrum of **6** with integration in blue.

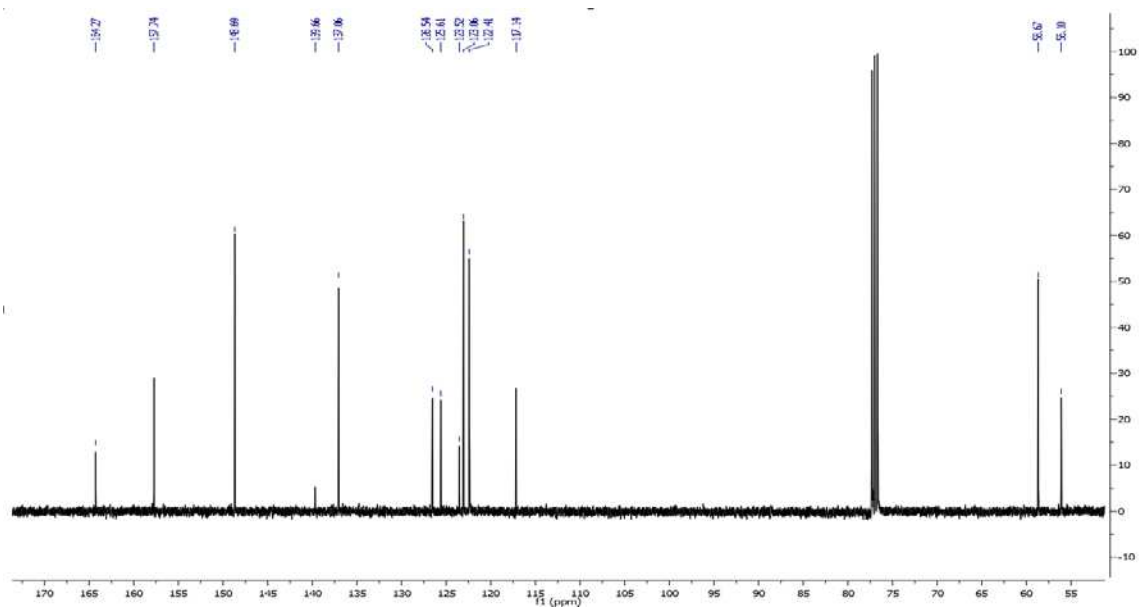


Figure A10. ¹³C NMR spectrum of **6**.

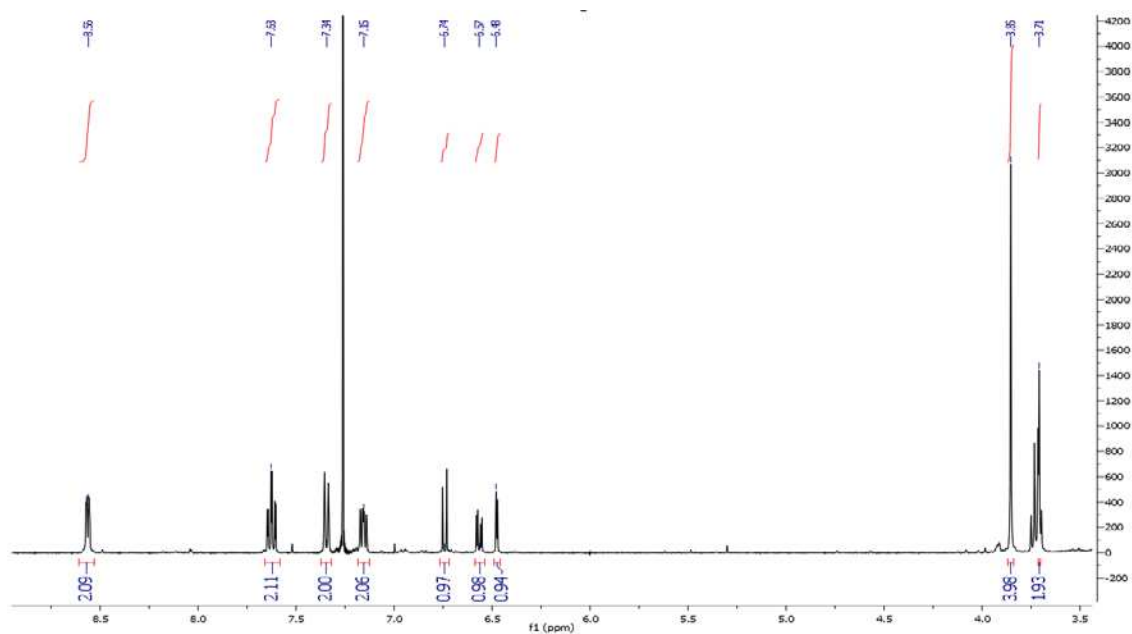


Figure A11. ^1H NMR spectrum of **7** with integration in blue.

Sample name: WZ 01

Exact mass of $\text{C}_{19}\text{H}_{19}\text{N}_4\text{OCl}_2\text{FeNa}^+$ = 468.017755 m/z

Observed Mass = 468.022828 m/z

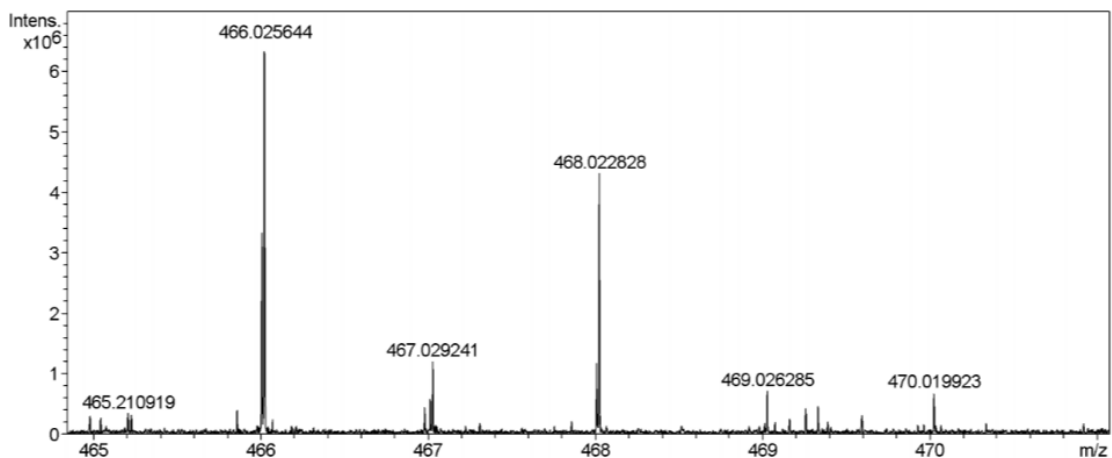


Figure A12. High-resolution mass spectrum of **8** in 1:1 THF:MeOH w/ NaCl. The expected molecular ions were observed.

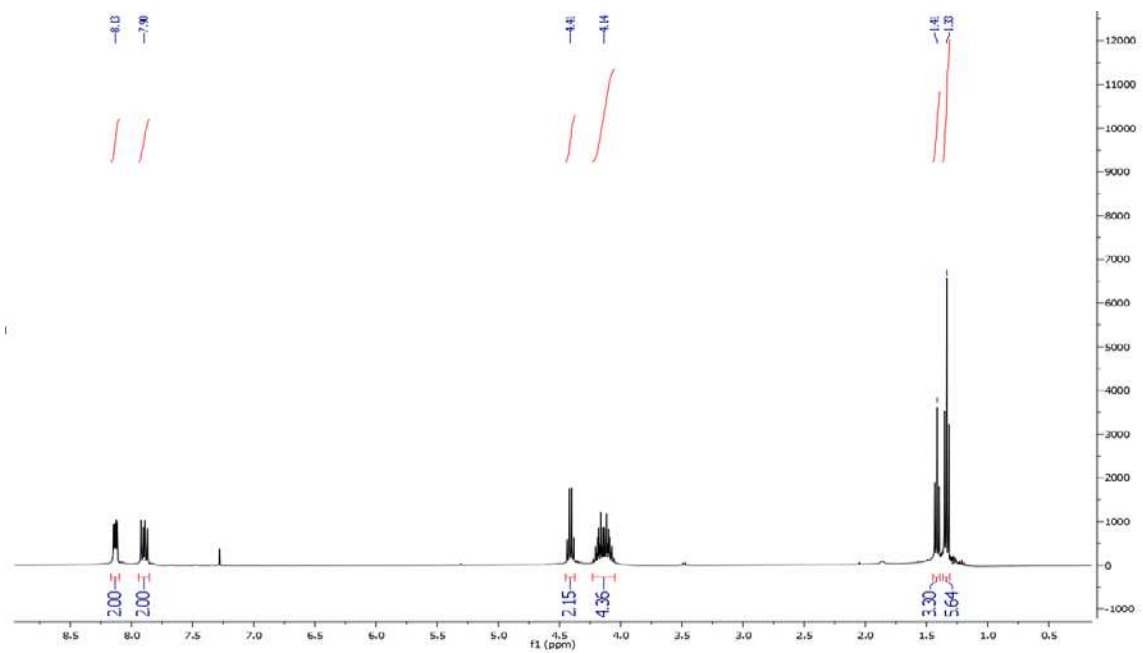


Figure A13. ^1H NMR spectrum of **9** with integration in blue.

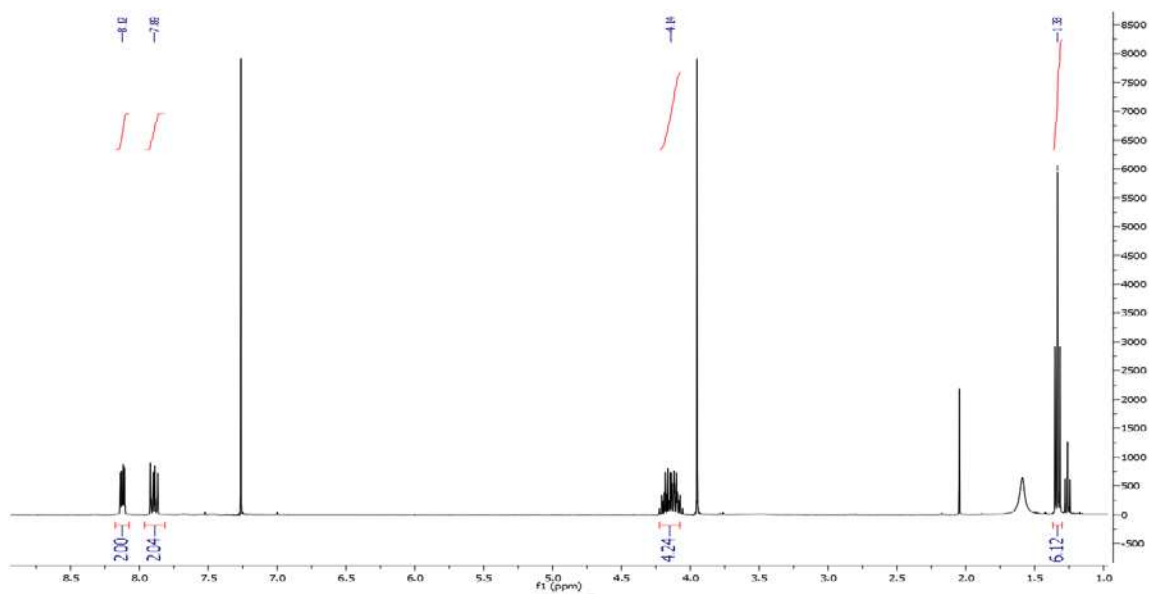


Figure A14. ^1H NMR spectrum of **10** with integration in blue.

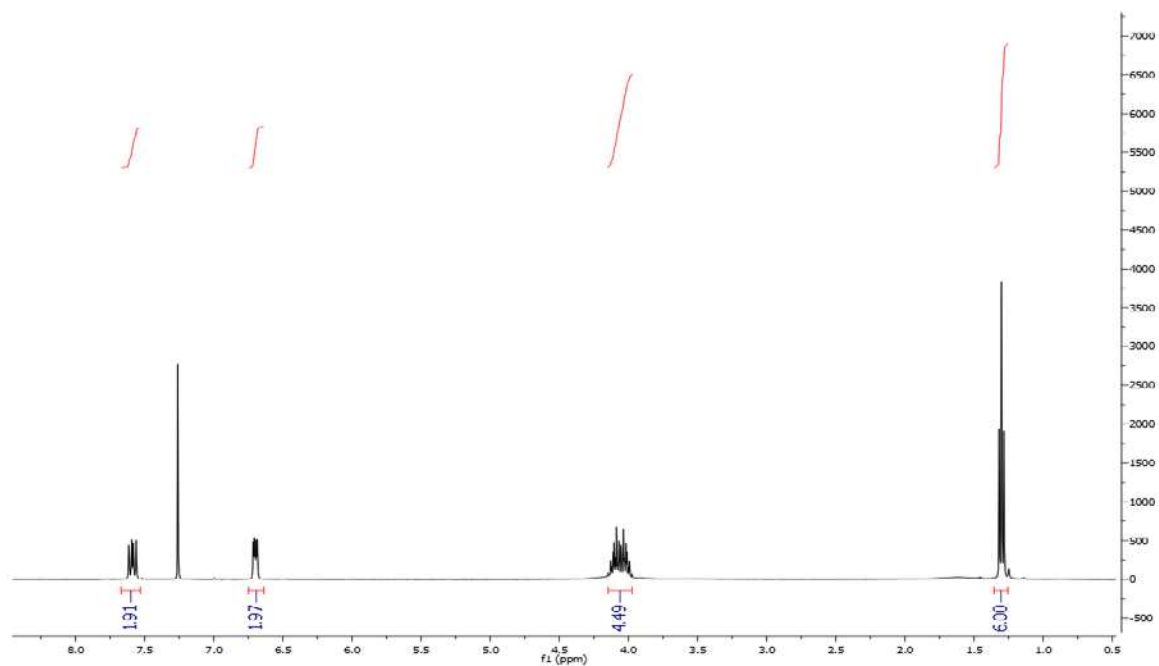


Figure A15. ^1H NMR spectrum of **11** with integration in blue.

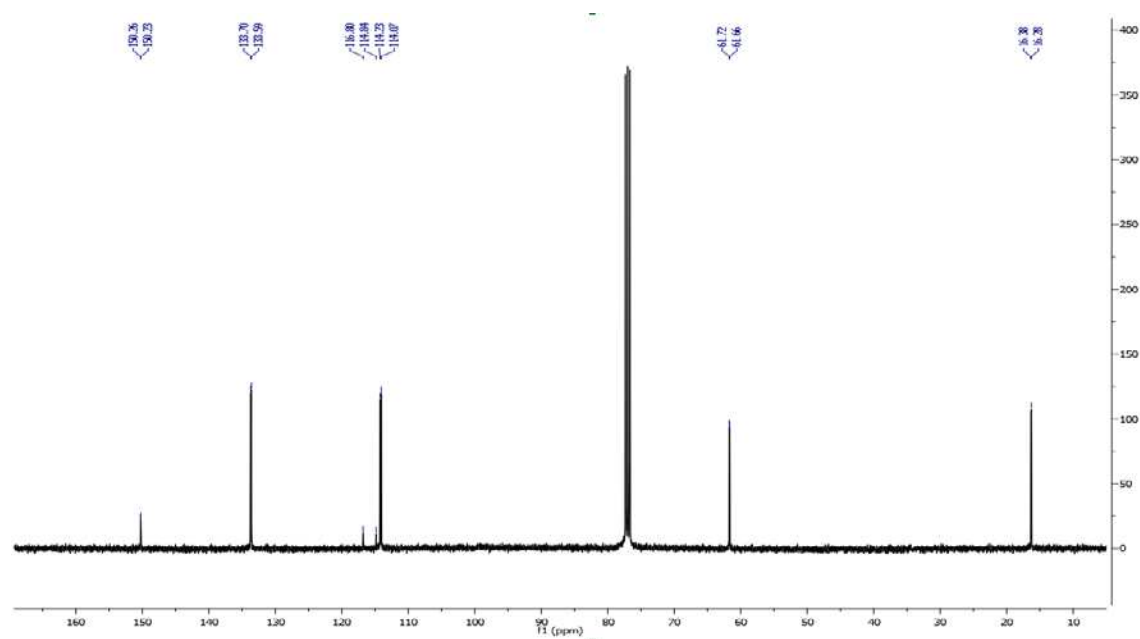


Figure A16. ^{13}C NMR spectrum of **11**.

Exact mass of $\text{C}_{30}\text{H}_{33}\text{N}_4\text{O}_5\text{PH}^+$ = 229.09 m/z
 Exact mass observed = 229.2 m/z

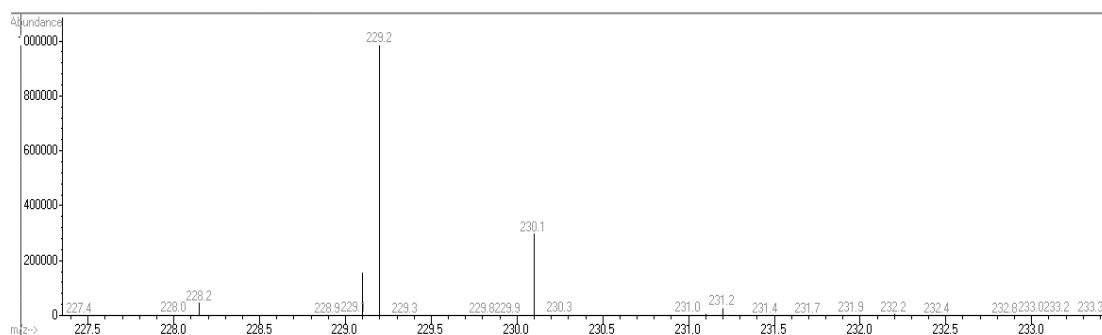


Figure A17. GC-MS spectrum of **11** in chloroform. The expected molecular ions were observed.

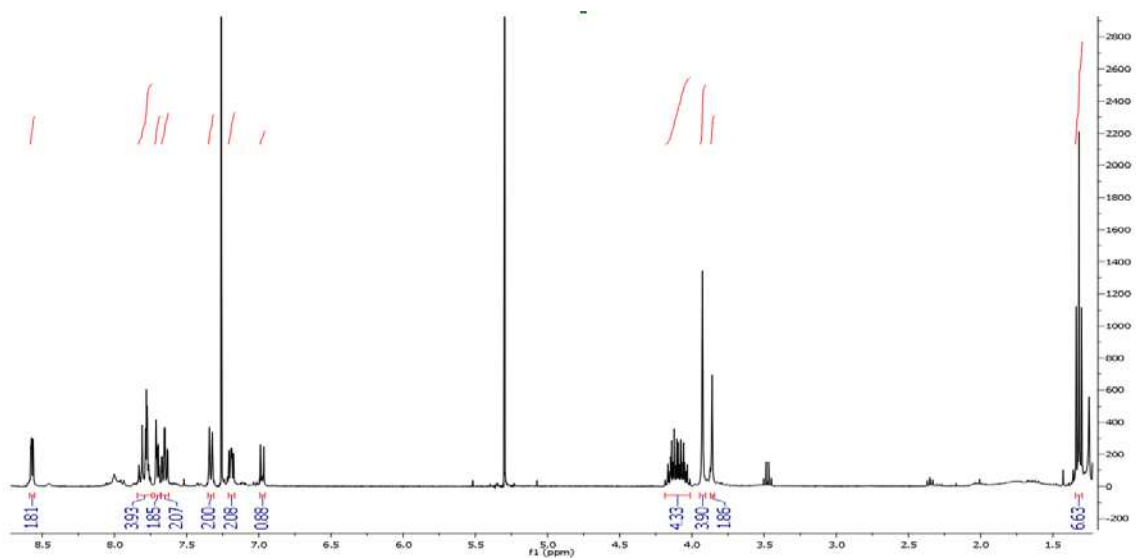


Figure A18. ^1H NMR spectrum of **12** with integrations in blue.

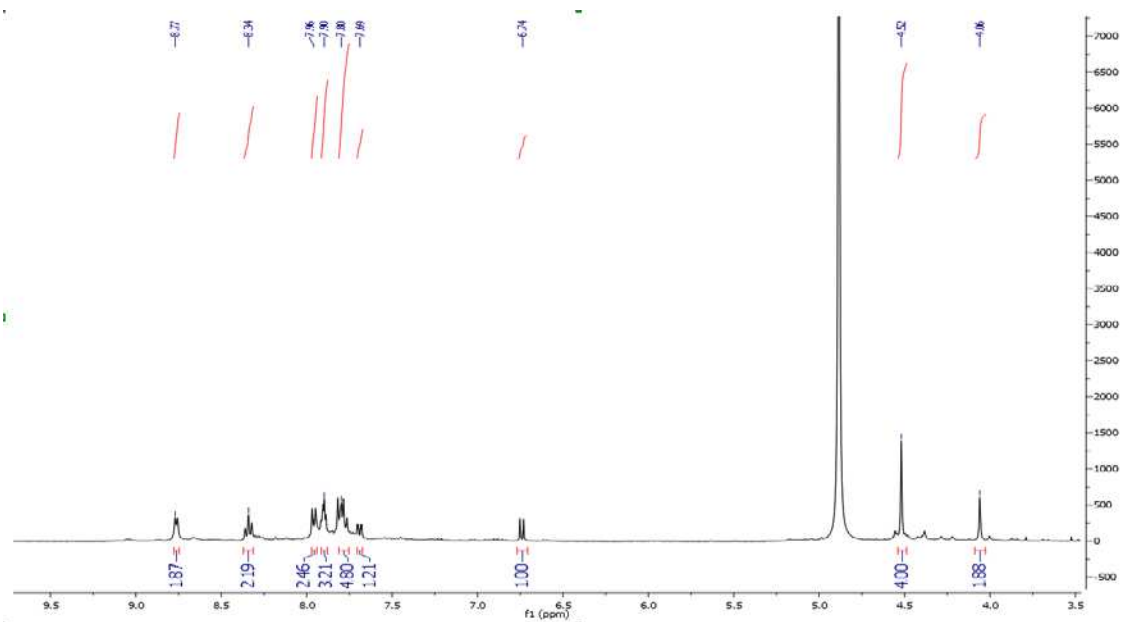


Figure A21. ¹H NMR spectrum of **13** with integrations in blue.

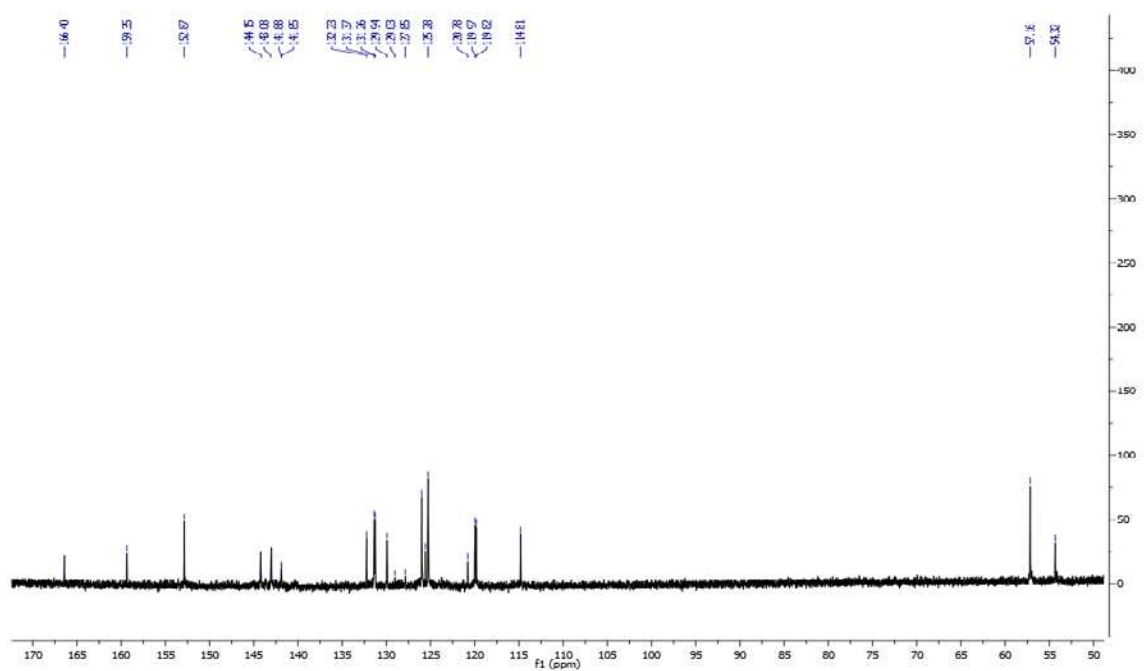


Figure A22. ¹³C NMR spectrum of **13**.

Sample name: WZ 06

Exact mass of $\text{C}_{26}\text{H}_{25}\text{N}_4\text{O}_5\text{PNa}^+$ = 505.163533 m/z

Exact mass observed = 505.163539 m/z

Difference = < 1.0 ppm

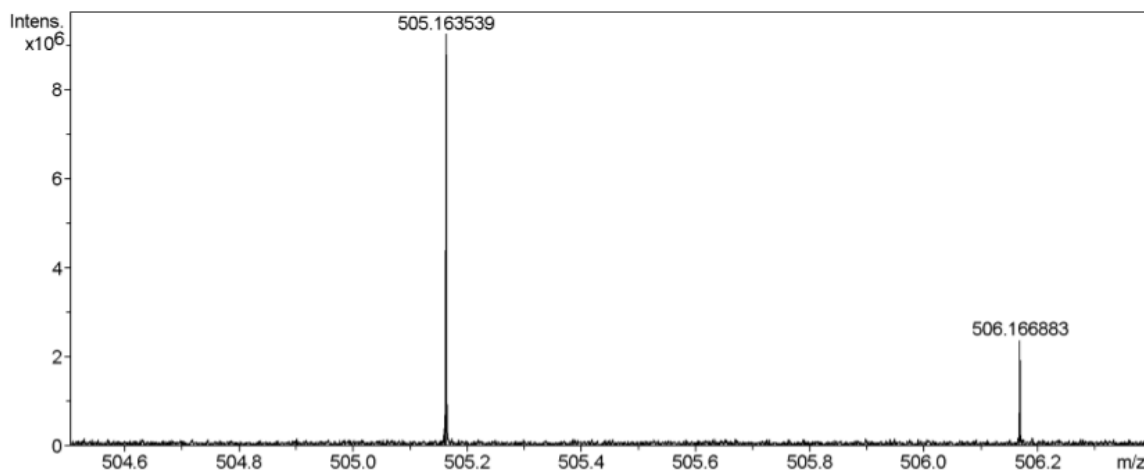


Figure A23. High-resolution mass spectrum of **13** in 1:1 THF:MeOH w/ NaCl. The expected molecular ions were observed with a difference of less than 1 ppm.

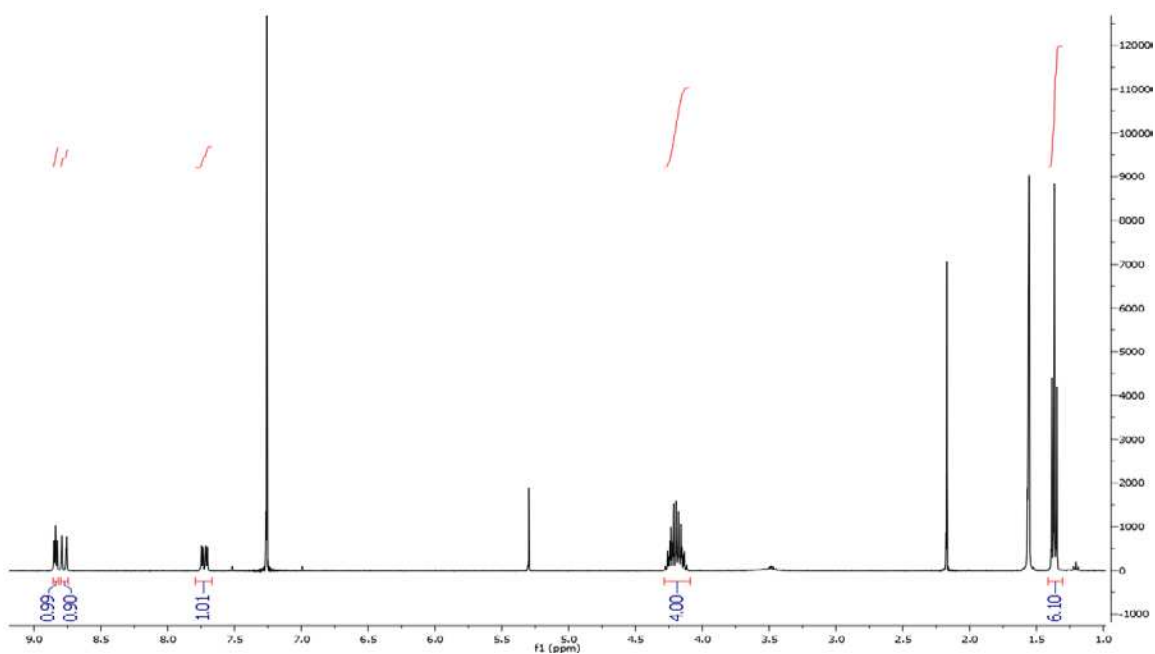


Figure A24. ¹H NMR spectrum of **14** with integrations in blue.

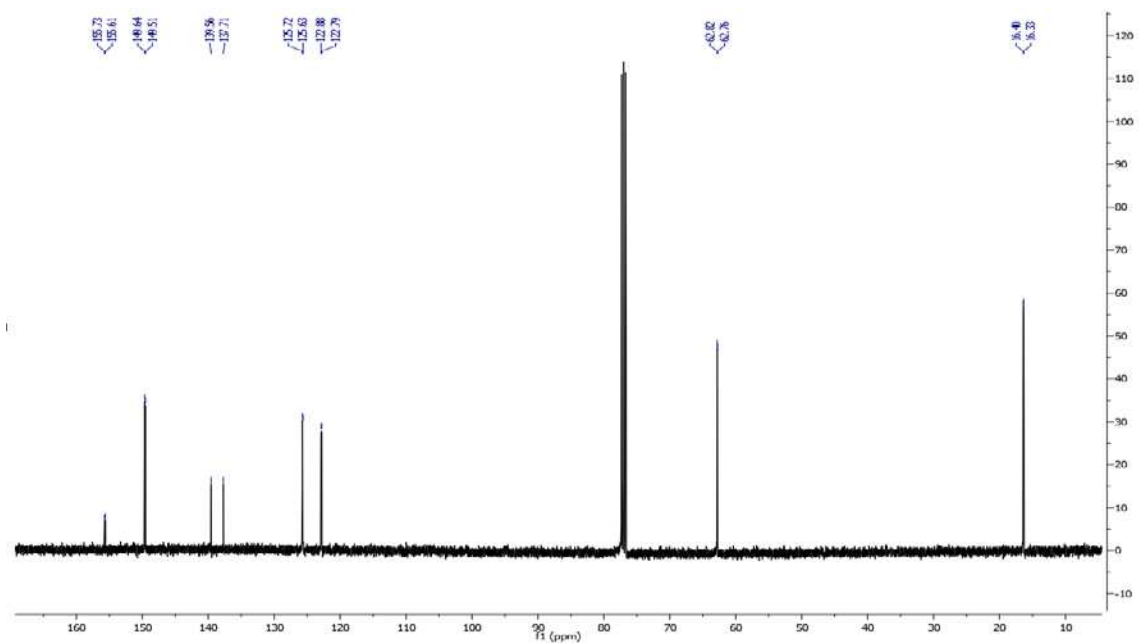


Figure A25. ^{13}C NMR spectrum of **14**.

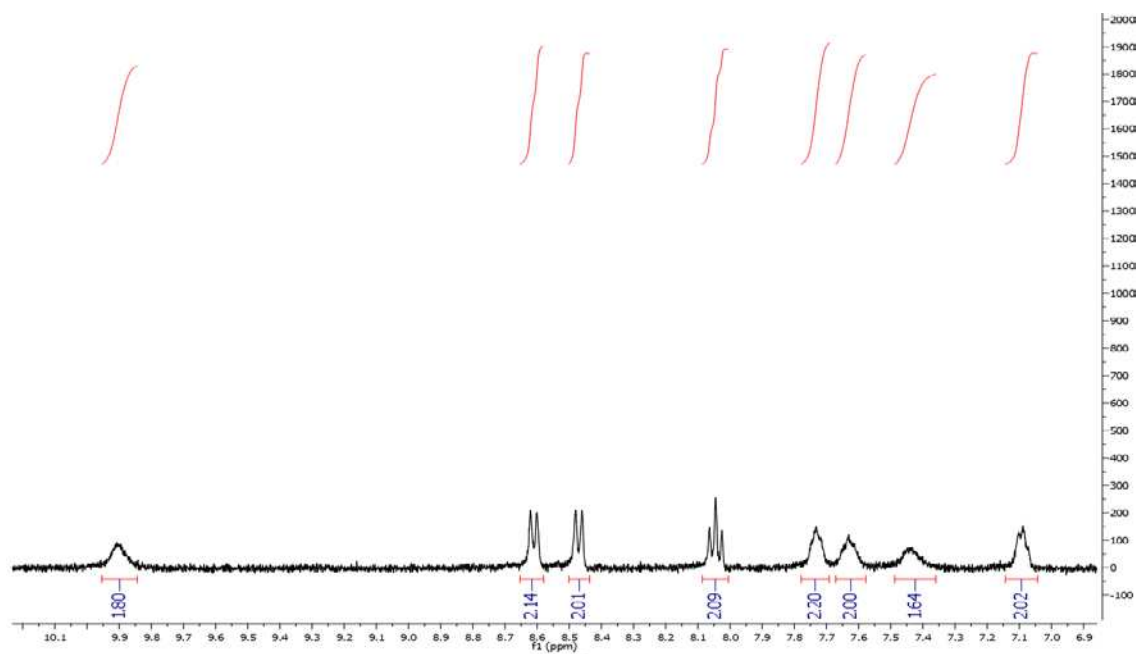


Figure A26. ^1H NMR spectrum of **15** with integrations in blue.

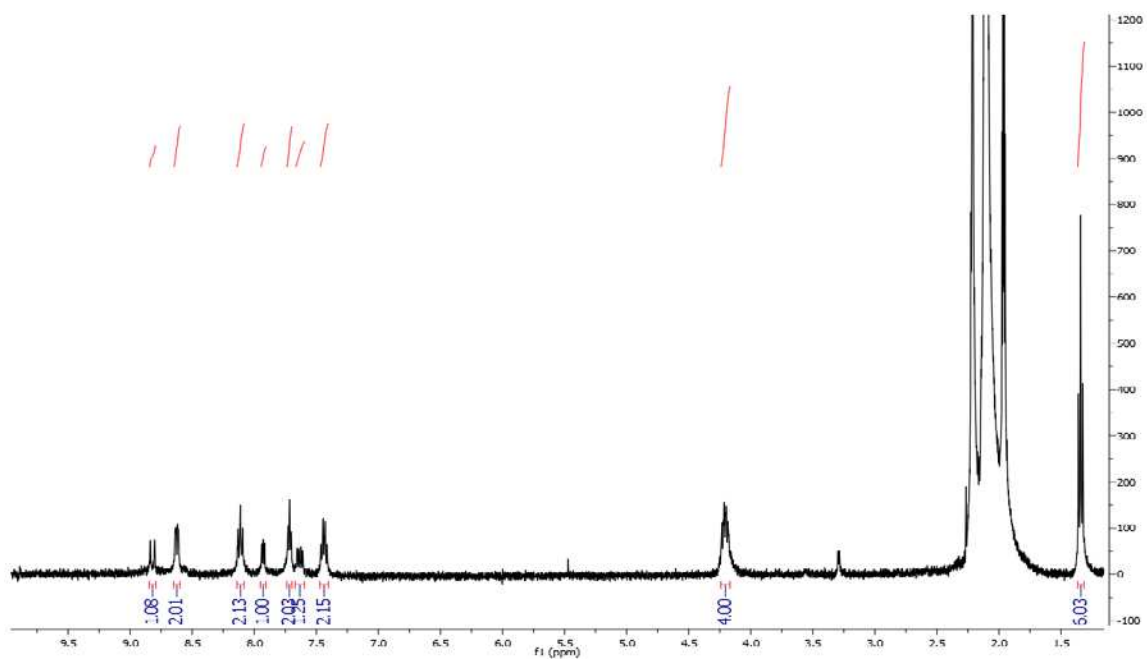


Figure A27. ^1H NMR spectrum of **16** with integrations in blue.

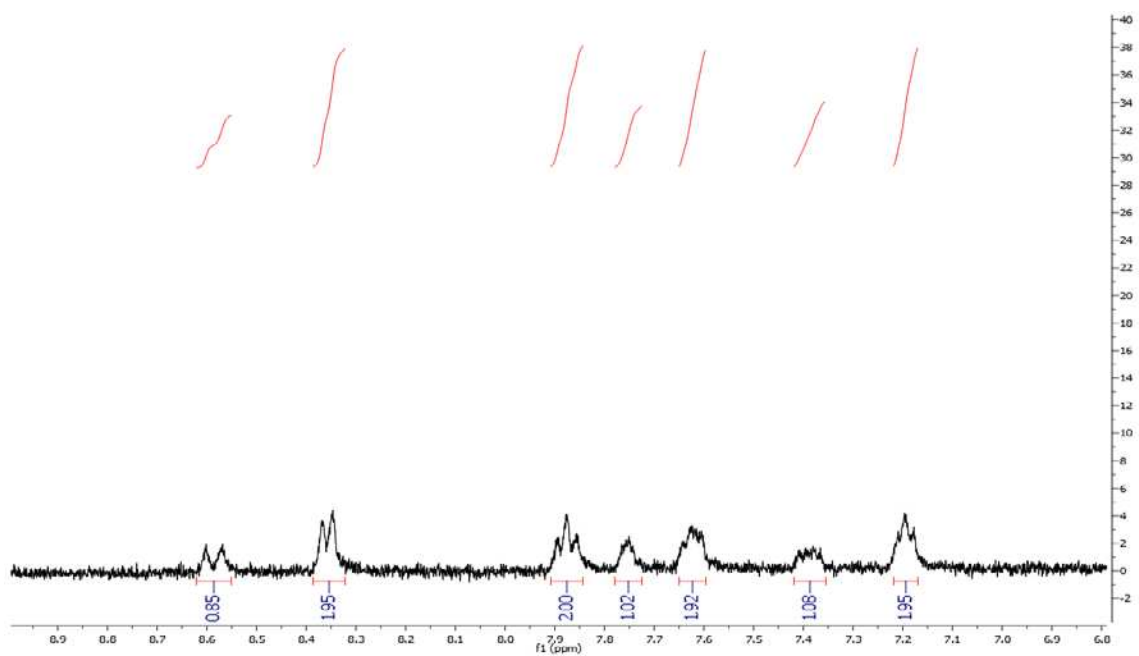


Figure A28. ^1H NMR spectrum of **17** with integration in blue.

Chapter 3 Photocatalytic Hydrogen Evolution from Water with the Iron Polypyridyl Catalyst on a Dye-Sensitized TiO₂ Nanoparticle

Introduction

Artificial Photosynthesis (AP) focuses on finding a way to harness solar energy to generate a chemical fuel.¹ Semiconducting materials, in particular TiO₂, are extensively studied as photocatalysts for AP due to relatively low cost and widespread use as an efficient charge-separating support.² In order to achieve efficient hydrogen production, TiO₂ nanoparticles need to be functionalized with a proton reducing catalyst to lower the overpotential of hydrogen evolution.³ While many first-row transition metal complexes have been reported to reduce protons electrocatalytically, few metal complexes have been investigated in a TiO₂-based photocatalytic system.

An effective means of testing the photocatalytic activity of the proton reduction catalyst involves incorporating the catalyst into a dye-sensitized TiO₂ nanoparticle. It was proposed that a catalyst/dye co-sensitized TiO₂ nanoparticle can operate by the following mechanism²: **RuP** (dye) absorbs visible light energy upon irradiation. The excited photosensitizer ejects electrons into the conduction band (CB) of TiO₂. Electrons are then transferred to the catalyst covalently attached to TiO₂, which drives the evolution of hydrogen. The redox cycle is completed by oxidation of the sacrificial electron donor triethanolamine (TEOA) and recovery of oxidized **RuP** (Figure 3.1). The feasibility of each step is determined by the excited state reduction potential of the photosensitizer, the CB of TiO₂, and the reduction potential for proton reduction.⁴

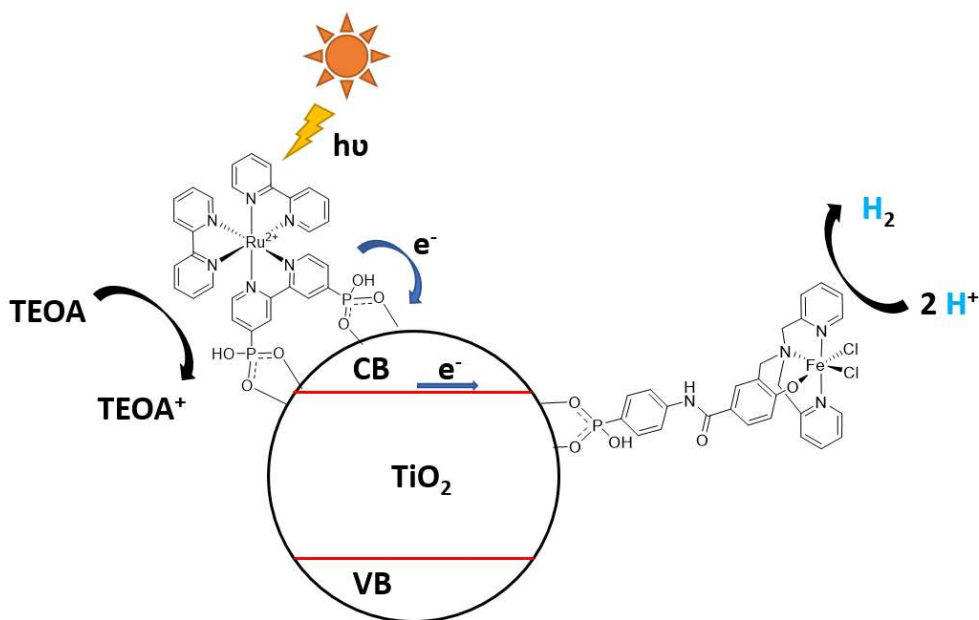


Figure 3.1. Schematic representation of photocatalytic hydrogen evolution with **[FeCl₂(L-P)]/RuP** sensitized TiO₂.

Previously, we reported an iron polypyridyl complex **[FeCl₂(L)]** that produces hydrogen electrocatalytically in pure aqueous solution at pH 3-5, with an overpotential of 800 mV.⁵ **[FeCl₂(L)]** also generates hydrogen photocatalytically from aqueous solvent in a homogeneous system consisting of a fluorescein photosensitizer, **[FeCl₂(L)]**, and TEA as the sacrificial electron donor. Because of the high catalytic activity and stability of **[FeCl₂(L)]** in aqueous environment, it was of interest to incorporate the catalyst into a dye-sensitized TiO₂ nanoparticle for photocatalytic hydrogen evolution.

The key requirement for the TiO₂-based photocatalytic system to work is that the catalyst **[FeCl₂(L)]** is covalently adsorbed to TiO₂.² In the previous chapter, **L-PO₃H₂** was successfully synthesized, allowing immobilization of the catalyst **[FeCl₂(L-PO₃H₂)]** on the TiO₂ surface via a phosphonic acid anchoring group. The work presented in this chapter continues the investigation of

[FeCl₂(L-PO₃H₂)] as a catalyst in a system employing TiO₂ semiconducting material for photocatalytic hydrogen evolution. The adsorption of **[FeCl₂(L-PO₃H₂)]** to TiO₂ nanoparticles was quantified by UV-vis spectroscopy. Photocatalytic activity of the **[FeCl₂(L-PO₃H₂)]/RuP** sensitized TiO₂ nanoparticles were investigated preliminarily for the feasibility of hydrogen evolution. The goal of this research is to develop a cost-effective iron complex as a hydrogen evolution catalyst on TiO₂, and ultimately allow for the preparation of a low-cost hydrogen evolving cathode in a photoelectrochemical water splitting cell.

Experimental Procedure

Sample preparation and experimental procedures are described below. All reagents not specifically mentioned were purchased from Acros Organics or Fisher Scientific without further purification. The Degussa P25 TiO₂ nanoparticles are 25 nm in diameter and are 70% anatase and 30% rutile. Triethanolamine (TEOA), triethylamine (TEA) and ascorbic acid (AA) stock solutions (0.10 M each) were titrated with 1 M HCl or NaOH to pH 7 at 25 °C. **L-PO₃H₂**, **RuP** and **[FeCl₂(L)]** were synthesized as described previously.

Instrumentation

¹H and ¹³C spectra were obtained using an Agilent 400MR DD2 spectrometer operating in the pulse Fourier transform mode. Chemical shifts are reported in ppm with the residual protio solvent as an internal reference. UV-vis spectra were recorded on a Cary 60 UV-vis spectrophotometer using samples dissolved in methanol. GC analysis was recorded on a Bruker Scion 436 gas chromatograph. pH readings were recorded using a Vernier LabQuest2 pH sensor.

Determine the molar extinction coefficient (ϵ) of **L-PO₃H₂**

L-PO₃H₂ solutions in methanol at concentrations of 8×10^{-6} M, 1.4×10^{-5} M, 2.0×10^{-5} M, 2.6×10^{-5} M, and 3.2×10^{-5} M were prepared. UV-vis spectra of the **L-PO₃H₂** solutions in a 1 cm cuvette were recorded on a Cary 60 UV-vis spectrophotometer. The spectrum of pure methanol (background) was subtracted from the spectra of the **L-PO₃H₂** solutions. Beer-Lambert Law is determined by

the following equation, where A is absorbance, ϵ is molar extinction coefficient, l is cell path length (cm) and c is the concentration of the **L-PO₃H₂** solution (M).

$$A = \epsilon / c \quad (3.1)$$

The absorbance of **L-PO₃H₂** solutions at 295 nm was plotted against the concentration. ϵ was determined by calculating the slope of the best-fit line. UV-vis spectra and calculations of ϵ are included in the text.

Adsorption of L-P to TiO₂ nanoparticles

L-PO₃H₂ (0.1 μ mol in 0.125 mL methanol) was added to a stirred dispersion of TiO₂ (5 mg in 0.375 mL methanol). The mixture was left stirring for 1 h and centrifuged at 13.4 rpm for 15 min. The clear supernatant was then analyzed by UV-vis spectrophotometry. The amount of **L-PO₃H₂** adsorbed to TiO₂ was quantified by the absorbance difference of the supernatant at 295 nm before and after exposure to TiO₂ nanoparticles.

Assembly of photocatalytic hydrogen production particles

FeCl₃·H₂O (0.1 μ mol in 0.1 mL methanol) was added to a stirred dispersion of TiO₂ sensitized with **L-PO₃H₂** (5 mg in 3.9 mL methanol). The mixture was left stirring for 1 h, and was subsequently and rinsed with methanol for 5 times. After the last rinse, **RuP** (0.1 μ mol in 0.1 mL methanol) was added to the stirred mixture of [**FeCl₂(L-PO₃H₂)**] sensitized TiO₂ nanoparticles (5 mg in 3.9 mL methanol). The mixture was left stirring for 1h, and was subsequently centrifuged, rinsed with methanol for 5 times. The TiO₂ nanoparticles co-

sensitized with **[FeCl₂(L-PO₃H₂)]** and **RuP** were dried in air, and Al foil protected the nanoparticles from light.

GC calibration

Two 500 mL round bottom flasks were filled with CH₄ and H₂ gas respectively, and sealed with septa secured with copper wire. A sample was then prepared in a test tube containing a solution of 2.0 mL of acetonitrile and 2.0 mL of DI water. The sample was sealed with a rubber septum, secured with copper wire, and degassed under Ar for approximately 15 minutes. A 10.0 mL Hamilton gastight syringe was then used to remove 1.0 mL of headspace gas from the test tube and 1.0 mL of CH₄ was added as an internal standard. Various amounts of H₂ gas, ranging from 10 μ L to 500 μ L, were then added to the test tube. Gas samples of 100 μ L each were injected into a GC to determine the ratio of peak areas of H₂ to CH₄. The peak area ratios were then plotted versus the volume of H₂. The slope of the linear trend of the data was used to calculate the volume of H₂ generated from hydrogen evolution studies (Figure 3.2).

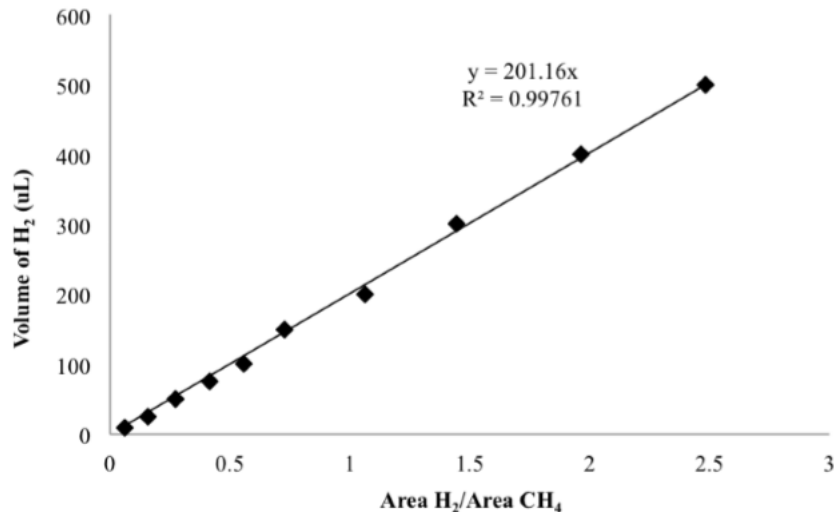


Figure 3.3. Calibration curve of H₂ to CH₄ peak areas used for determination of hydrogen generation. The ratio of peak areas was plotted against the volume of H₂ injected into the GC.

Photocatalytic hydrogen evolution

All hydrogen evolution studies were conducted by preparing 16.0 mm × 125.0 mm glass test tubes with 5 mg of [FeCl₂(L-PO₃H₂)] /RuP co-sensitized TiO₂ nanoparticles and 4 mL of stock solution of electron sacrificial donor in DI water (0.1 M) with a micro-stir bar, unless noted otherwise. Test tubes were sealed with septa, secured with copper wire, and shielded from light with Al foil. The test tubes were degassed for 15 min under Ar. 1.0 mL of gas from the headspace of each test tube was removed using a 10.0 mL Hamilton gastight syringe, and 1.0 mL of CH₄ gas was added to each cell as an internal standard. The test tubes were inserted into a custom-built holder attached to a small motor that spins samples at 3 revolutions/min above a stir plate, and irradiated in a green LED apparatus (λ = 520 nm, P = 0.12 W). LEDs of this wavelength were selected

because a broad range of photosensitizers can absorb light energy at 520 nm. A fan cooled the assembly to maintain 22°C in the apparatus during the experiment. Hydrogen generation was measured using GC analysis by removing a sample of 100 µL of gas from the headspace of each test tube. For the control experiments, hydrogen evolution studies were performed with the absence of either TiO₂, **L-PO₃H₂**, FeCl₃, or TEOA (sacrificial donor). See Table 3.1.

Results and Discussions

Quantify the adsorption of L-PO₃H₂ to TiO₂ nanoparticles

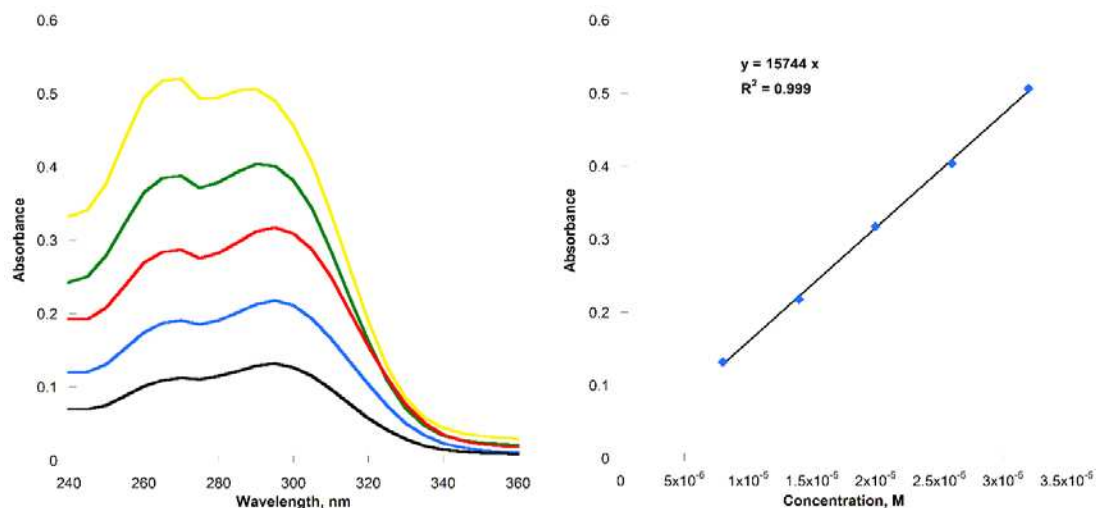


Figure 3.4. *Left:* UV-vis spectrum of **L-PO₃H₂** solution in methanol at concentrations of 8×10^{-6} (black), 1.4×10^{-5} (blue), 2.0×10^{-5} (red), 2.6×10^{-5} (green), 3.2×10^{-5} (yellow). *Right:* Absorption at 295 nm vs. concentration of **L-PO₃H₂**.

The UV-vis spectrum of **L-PO₃H₂** solution in methanol shows absorption at $\lambda = 205$ nm (π - π^* transition) and $\lambda = 295$ nm (π - π^* transition) (Figure 3.3 *Left*). The maximum visible absorbance at $\lambda = 295$ nm was plotted against the concentrations of the **L-PO₃H₂** solution respectively. According to the Beer-Lambert Law, the fraction of the light absorbed by each layer of solution is the same. Therefore, the plot of absorbance against concentration should exhibit a linear trend. The slope of the best-fit line was used to determine the molar extinction coefficient (ϵ) of **L-PO₃H₂** (Figure 3.3 *Right*).

$$\epsilon = 1.57 \times 10^4 \text{ L mol}^{-1} \text{ cm}^{-1}$$

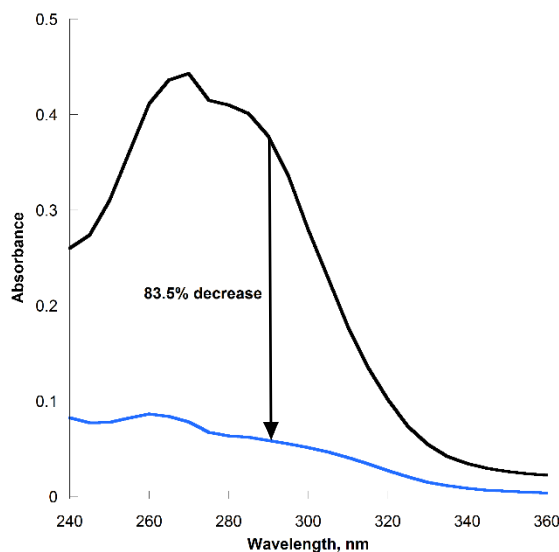


Figure 3.5. UV-vis spectrum of **L-PO₃H₂** (2.5×10^{-5} M) (in the absence of TiO₂; black) and the supernatant after stirring with TiO₂ (5 mg in 4 mL of MeOH) for 1 h following centrifugation (blue).

The adsorption of **L-PO₃H₂** to TiO₂ nanoparticles was quantified by the UV-vis absorption at $\lambda = 295$ nm. Figure 3.4 shows the UV-vis spectrum of **L-PO₃H₂** (0.1 μ mol) in the absence of TiO₂ and after stirring with TiO₂ (5 mg). After stirring with TiO₂, the absorbance at 295 nm decreases by 83.5%. Therefore, the phosphonate linkers allowed for the adsorption of approximately 83.5% of 0.1 μ mol **L-PO₃H₂** on TiO₂ nanoparticles. In the photochemical experiments, it was assumed that 100% of the **L-PO₃H₂** attached to TiO₂ nanoparticles reacted with FeCl₃ to form **[FeCl₂(L-PO₃H₂)]**. The phosphonate anchor of **RuP** allow for the quantitative attachment (> 95%) of the photosensitizer to TiO₂ nanoparticles.⁶

Photocatalytic hydrogen evolution with $[\text{FeCl}_2(\text{L-PO}_3\text{H}_2)]/\text{RuP}$ sensitized TiO_2

In order to determine the most suitable sacrificial electron donor for the photochemical system, visible-light driven hydrogen evolution was obtained with a loading of 0.1 μmol of $[\text{FeCl}_2(\text{L-PO}_3\text{H}_2)]$ and 0.1 μmol of **RuP** on 5 mg Degussa P25 TiO_2 in TEOA, TEA or AA solution in water (4 mL, 0.1 M) at pH 7 (Table 3.1). The experiments with TEA and AA only generated negligible amounts of hydrogen. Therefore, TEOA was used for the rest of the standard experiments and control experiments.

The standard conditions for visible-light driven hydrogen evolution was obtained with a loading of 0.1 μmol of $[\text{FeCl}_2(\text{L-PO}_3\text{H}_2)]$ and 0.1 μmol of **RuP** on 5 mg Degussa P25 TiO_2 in TEOA solution in water (4 mL, 0.1 M) at pH 7 (Table 3.1). The photocatalytic system generated 130 μL hydrogen gas in 22 h. This corresponds to a turnover number (TON) of 70 mol H_2 (mol $[\text{FeCl}_2(\text{L-PO}_3\text{H}_2)]$)⁻¹.

In the absence of TEOA, TiO_2 , or FeCl_3 , only negligible amounts of hydrogen were detected (Table 3.1). In addition, no hydrogen evolution was observed when both **L-PO₃H₂** and TiO_2 were absent. This control experiment demonstrates that **RuP** does not promote evolution of hydrogen from FeCl_3 nanoparticles although other workers have reported hydrogen generation from FeCl_3 nanoparticles in unrelated systems. In the absence of FeCl_3 , the system generated a modest amount of hydrogen. This is most likely because **L-PO₃H₂** reacted with FeCl_3 impurities and formed the catalyst $[\text{FeCl}_2(\text{L-PO}_3\text{H}_2)]$ during sample preparation.

Table 3.1. Photocatalytic Hydrogen Evolution with **[FeCl₂(L-PO₃H₂)]** and **RuP** attached to TiO₂ Nanoparticles at pH 7

#	Catalytic Nanoparticle System	Experimental Conditions	H ₂ (μL)	TON
<i>Standard system- electron transfer from RuP to [FeCl₂(L-PO₃H₂)]</i>				
1	[FeCl₂(L-PO₃H₂)] (0.1 μmol), RuP (0.1 μmol), TiO ₂ (5 mg)	TEOA, visible light	130	70
<i>Sacrificial donor variation</i>				
2	[FeCl₂(L-PO₃H₂)] (0.1 μmol), RuP (0.1 μmol), TiO ₂ (5 mg)	TEOA, visible light	7	4
3	[FeCl₂(L-PO₃H₂)] (0.1 μmol), RuP (0.1 μmol), TiO ₂ (5 mg)	TEA, visible light	0.2	0.1
4	[FeCl₂(L-PO₃H₂)] (0.1 μmol), RuP (0.1 μmol), TiO ₂ (5 mg)	AA, visible light	---	---
<i>Control Experiments</i>				
5	no L-PO₃H₂ , FeCl ₃ (0.1 μmol), RuP (0.1 μmol), no TiO ₂	TEOA, visible light	---	---
6	no L-PO₃H₂ , FeCl ₃ (0.1 μmol), RuP (0.1 μmol), TiO ₂ (5 mg)	TEOA, visible light	6	3
7	L-PO₃H₂ (0.1 μmol), no FeCl ₃ , RuP (0.1 μmol), TiO ₂ (5 mg)	TEOA, visible light	49	26
8	[FeCl₂(L-PO₃H₂)] (0.1 μmol), RuP (0.1 μmol), TiO ₂ (5 mg)	no TEOA, visible light	---	---
9	[FeCl₂(L)] (0.1 μmol), RuP (0.1 μmol), no TiO ₂ ^a	TEOA, visible light	---	---

(a) The parent complex **[FeCl₂(L)]** was used because pure **[FeCl₂(L-PO₃H₂)]** could not be isolated

Conclusion

The work in this chapter establishes a standardized procedure for sensitized TiO₂ nanoparticle preparation and heterogeneous photochemical experiments. The molar extinction coefficient of **L-PO₃H₂** is determined to be $1.57 \times 10^4 \text{ L mol}^{-1} \text{ cm}^{-1}$, and 83.5% of **L-PO₃H₂** (0.1 μmol) can be adsorbed onto TiO₂ nanoparticles (5 mg) after stirring for 1 h. In the preliminary photochemical experiments, TEOA is established as the most suitable sacrificial electron donor for the TiO₂-based photocatalytic system. **[FeCl₂(L-PO₃H₂)]/RuP** sensitized TiO₂ nanoparticles evolve hydrogen with a TON of 70 under standard condition (Table 3.1). This promising result shows that **[FeCl₂(L-PO₃H₂)]** is very likely an active catalyst for TiO₂-based photocatalytic hydrogen evolution. While future research is needed to determine the optimum conditions for visible-light driven hydrogen evolution, the work presented in this thesis demonstrates that the incorporation of an earth-abundant iron catalyst onto TiO₂ is a promising method toward developing a practical device for AP.

References

1. (a) Ni, M.; Leung, M. K. H.; Leung, D. Y. C.; Sumathy, K., A Review and Recent Developments in Photocatalytic Water-Splitting Using for Hydrogen Production. *Renewable and Sustainable Energy Reviews* **2007**, *11* (3), 401-425; (b) Barber, J.; Tran, P. D., From Natural to Artificial Photosynthesis. *J. R. Soc. Interface* **2013**, *10* (81), 20120984/1-20120984/16.
2. Lakadamyali, F.; Reisner, E., Photocatalytic H₂ Evolution from Neutral Water with a Molecular Cobalt Catalyst on a Dye-Sensitized TiO₂ Nanoparticle. *Chem. Commun. (Cambridge, U. K.)* **2011**, *47* (6), 1695-1697.
3. Linsebigler, A. L.; Lu, G.; Yates, J. T., Jr., Photocatalysis on TiO₂ Surfaces: Principles, Mechanisms, and Selected Results. *Chem. Rev.* **1995**, *95* (3), 735-58.
4. Eckenhoff, W. T.; McNamara, W. R.; Du, P.; Eisenberg, R., Cobalt Complexes as Artificial Hydrogenases for the Reductive Side of Water Splitting. *Biochimica et Biophysica Acta (BBA) - Bioenergetics* **2013**, *1827* (8-9), 958-973.
5. Connor, G. P.; Mayer, K. J.; Tribble, C. S.; McNamara, W. R., Hydrogen Evolution Catalyzed by an Iron Polypyridyl Complex in Aqueous Solutions. *Inorganic Chemistry* **2014**, *53* (11), 5408-5410.
6. Lakadamyali, F.; Reynal, A.; Kato, M.; Durrant, J. R.; Reisner, E., Electron Transfer in Dye-Sensitized Semiconductors Modified with Molecular Cobalt Catalysts: Photoreduction of Aqueous Protons. *Chem. Eur. J.* **2012**, *18* (48), 15464-15475, S15464/1-S15464/18.